

0203
DREV R-660/72

PROJ. 95-51-10

NON CLASSIFIÉ
UNCLASSIFIED

040
X_S-BAND MICROWAVE INTERFEROMETER FOR STUDY OF
HYPERSONIC TURBULENT WAKE ON RANGE 5

1101 1102 1103
N. Gagné, A. Fitchett, D. Heckman

07 CAN
1911 51
1102 16
35 D-95-51-10



CENTRE DE RECHERCHES POUR LA DÉFENSE

DEFENCE RESEARCH ESTABLISHMENT

VALCARTIER

0204
DEFENCE RESEARCH BOARD

0204b Valcartier QUE (CAN)
CONSEIL DE RECHERCHES POUR LA DÉFENSE

Québec, Canada

46 November/novembre 1972

DC

DREV R-660/72
PROJ: 95-51-10

NON CLASSIFIE
UNCLASSIFIED

16537

X_S-BAND MICROWAVE INTERFEROMETER FOR STUDY OF
HYPERSONIC TURBULENT WAKE ON RANGE 5

by

N. Gagné, A. Fitchett, D. Heckman

CENTRE DE RECHERCHES POUR LA DEFENSE
DEFENCE RESEARCH ESTABLISHMENT
VALCARTIER
Tel: (418) 844-4271

Québec, Canada

November/novembre 1972

RESUME

Les recherches ayant pour but la détermination des charges électriques moyennes et variables dans les traînées ionisées de projectiles hypersoniques nécessitent l'emploi d'un interféromètre micro-onde de la bande X_S . Un interféromètre de ce type installé dans le tunnel de tirs hypersoniques n° 5 du Centre de recherches pour la défense, Valcartier (CRDV) a été utilisé pour obtenir une autre estimation de la densité moyenne d'électrons libres. A l'aide d'un système de deux lentilles bornant la trajectoire, on a obtenu des faisceaux de deux pouces de diamètre. Ce rapport décrit le système diffuseurs-lentilles, les systèmes de transmission et de réception des signaux ainsi que les méthodes d'étalonnage et d'analyse. Généralement, les expériences dans les tunnels de tirs balistiques comprennent des mesures plutôt arbitraires des électrons libres dans des volumes aussi indéfinis. Ici, nous allons plus loin. En assumant une distribution gaussienne de la densité des électrons libres dans la traînée et en employant un système à double faisceaux, on déduit l'amplitude par rapport à un espace donné en fonction du temps ou de la distance à l'arrière du projectile. On inclut des résultats typiques obtenus lors du lancement d'un projectile sphérique de 2.7 pouces de diamètre dans une atmosphère d'air raréfié à 14,500 pieds à la seconde.

ABSTRACT

50 As part of a research program aimed at determining the behavior of the mean and fluctuating charge density levels in an ionized turbulent wake, a dual channel microwave interferometric equipment operating at X_S -Band has been installed on the hypersonic Range 5 facility at Defence Research Establishment, Valcartier (DREV) to provide an independent estimate of the mean electron density. Resolution of the order of 2 inches is provided by a double-lens focussing system, installed about the projectile line-of-flight. The present report describes in detail the horn-lens system, the transmission and receiving systems, and the calibration and analysis procedures. The analysis employed here goes somewhat beyond the conventional ballistic range practice of quoting a result indicative of the integration of a somewhat arbitrary electron density over an equally indefinite path length. Instead, on the basis of an assumed gaussian electron density distribution in the wake, the two measurements made with the dual channel equipment are used to infer both the amplitude and the width parameters of the assumed distribution function as a function of time or axial distance behind the projectile. Typical results are presented for the case of 2.7 inch diameter spheres flown at 14,500 feet/second in air.

TABLE OF CONTENTS

	RESUME/ABSTRACT	i
1.0	INTRODUCTION	1
2.0	THE INTERFEROMETER EQUIPMENT	2
	2.1 General	2
	2.2 From the Microwave Oscillator to the Transmission Reference Arms	3
	2.3 Transmission Arms	4
	2.4 Horn-Lens System	5
	2.5 The Receiver System	8
	2.6 Detector and Amplification Network	9
	2.7 Recording	9
3.0	CALIBRATION PROCEDURE	10
4.0	ANALYSIS	12
	4.1 Determination of Transmission Arm Phase Shifts	12
	4.2 Characteristics of Wake Electron Density Distribution	14
5.0	RESULTS	17
	5.1 Typical Data	17
	5.2 Comparison with Outside Ballistic Range Data	18
	5.2.1 Transformation of GM ACDRL Data	18
	5.2.2 Transformation of MIT Lincoln Laboratory Data	19
	5.2.3 Comparison with Theoretical Calculations of AVCO	19
	5.2.4 Results of Comparison of Data	20
6.0	CONCLUSIONS	20
7.0	ACKNOWLEDGEMENTS	21
	REFERENCES	23
	APPENDIX A: Design Considerations for Dielectric Focussing Lens System for Range 5 Interferometer	57
	A.1 Double Lens Focussing System	57
	A.2 Reflected Shock Considerations	57
	A.3 Mechanical Rigidity	58
	A.4 Scaling a Lens Design	58
	A.5 Detailed Lens Design	59

1.0 INTRODUCTION

Since 1965, the Defence Research Establishment, Valcartier (DREV) has been carrying out a large program of experimental measurements aimed at determining the mean and fluctuating properties of various physio-chemical variables in the hypersonic turbulent wake (Ref. 1). Instrumentation has been developed and applied to measure the spatial distribution of such variables as velocity, mean density, temperature, and charge density (Ref. 2-5). The properties of electron density are particularly interesting because they determine the character of the interaction of microwave radiation with such a wake.

At DREV, charge density measurements have been attempted using both Langmuir electron probes and electrostatic continuum ion probes (Ref. 5). The use of Langmuir probes is advantageous because of the simplicity of interpretation of probe currents in terms of mean and fluctuating electron density. However, electro-mechanical considerations make it difficult to contemplate the employment of large numbers of such probes simultaneously. On the other hand, continuum ion probes are simple, rugged and adapted to use in large multi-probe arrays; unfortunately their use has been discounted in most quarters because of the difficulties associated with the theoretical interpretation of the probe current. For a continuum probe, the probe current can apparently depend not only on ion density, but also on the temperature and fluid motion of the media in which the probe is immersed (Ref. 6).

One obvious approach to the intelligent use of ion probes is to attempt to investigate their behavior in a plasma which simulates condition encountered in the wake. This is the route chosen at DREV, where supplementary investigations have been carried out of ion probe behavior using the wake itself as the laboratory plasma. In any such investigation of the dependence of probe current on the charge density in the surrounding medium, there is a requirement for an independent means of estimating the charge density. There are two commonly utilized microwave instruments for estimating electron density in a medium; they are the interferometer or bridge and the microwave resonant cavity.

The microwave interferometer is a well known instrument capable of measuring integrated electron densities in the range from 10^{13} to about 10^{10} electrons centimeter⁻³ (Ref. 7). Cavity techniques have been exploited at MIT (Ref. 8) and elsewhere (Ref. 9) to measure integrated electron densities in the range from 10^{10} to about 10^7 electrons centimeter⁻³. Neither instrument produces a point measurement of electron density; in both cases what is measured is some sort of integrated electron density along a line or over a sensitive volume of the instrument, and supplementary information must be introduced to produce a true electron density estimate. Of course in order to estimate ion density from an electron density measurement, some additional assumptions are called for.

Effort was initiated on both the microwave interferometer and the microwave cavity techniques at DREV. While most of the hardware was purchased for both equipments, time and manpower were sufficient only for the implementation of the interferometer technique. This was unfortunate because the Langmuir probe data measured at DREV, for example, extends to over 2000 diameters, and is only overlapped by the interferometer data to about 400 diameters. Nevertheless the interferometer installed at DREV has provided valuable data on both types of probe behavior and also on the properties of the wake. The purpose of this report is to describe in detail the DREV Range 5 interferometer and to illustrate the quality of the data which can be obtained.

2.0 THE INTERFEROMETER EQUIPMENT

2.1 General

The present technical report is concerned with the X_S-Band microwave interferometer installed at station 272.0 feet on DREV Hypersonic Facility Range 5 (Fig. 1). The experimental equipment occupies all of one five foot bay from 270 to 275 feet on both sides of the range or flight tank. The transmitter, associated high voltage and timing equipment, and some of the recording instrumentation is situated on the free-access (north) side of the range (Fig. 2), while the receiver/detectors, reference-balance networks and summation and line driver modules are on the south side (Fig. 3). A simplified block diagram of the interferometer is shown in Figure 4.

Basically, the equipment consists of an X_S-Band source feeding a transmission and reference arm (Ref. 10). The transmitted signal is pulsed 'off' for a short duration as a calibration procedure and for the zero (dc null) determination. After power division, the transmitted signal is fed to a dual conical horn antenna array. The horns are cross polarized to minimize cross-talk and act as a beam fence with the beam axes situated equally on either side of the flight axis. The dual-beam configuration allows for a larger coverage of the flight axis than would be possible with a single channel and as such, acts as a palliative against round-to-round dispersion. In this regard, the present system falls short of similar equipments which use up to seven beams, (in fact spherical and other aberrations introduced by extreme off-axis illumination in these latter equipments seriously affect the data and must be compensated for in the analysis unless modifications to the lens system can be introduced to offset these affects).

In addition to the increased coverage, the dual beam configuration permits a somewhat different analysis procedure to be followed than that for a single beam. By exploiting the dependence of the phase shift measured in each of the channels on the radial distance from the wake axis, it is possible to derive the parameters of an assumed gaussian distribution of electron density in the wake (Section 4.0). This technique is possible as long as the projectile does not pass exactly the same distance from both beams.

The horn array illuminates a standard single-pass, dual-focussed lens configuration (Fig. 5) from a source point located at twice the focal length or $L_1 = 2f$. This produces an image focal point at the same distance, i.e. on the range flight axis. At this focus, microwave energy interacts with the wake; it is then refocussed by the second lens onto the receiver horn array and compared to the unmodulated, unprocessed reference signal routed circumferentially around the lower part of the range tank.

Setting of the SINE-COSINE detection modes is determined by the phase and amplitude settings performed in individual reference channel arms feeding the separate mixer detectors. Normally, both modes can be recorded in each of the channels.

2.2 From the Microwave Oscillator to the Transmission Reference Arms

The microwave transmitter source is operated in the X_S -Band at 9.60 GHz ($\lambda = 3.1227$ cm.). The source, a convection-cooled, Varian V-58 0.5 watt reflex klystron operating in the 3-3/4 mode, is guide-launched in the dominant TE_{10} mode for WR-90 standard rectangular waveguide. The source power supply is a Hewlett Packard Model 416B unit with integrated beam, reflector, and filament supplies. Range constraints, which dictated a somewhat longer reference arm than was considered desirable from a standpoint of frequency sensitivity, necessitated the incorporation of a phase-lock network. This was provided in the form of a Microwave Specialties MOS-1 Stabilizer operating through the reflector circuit. This unit operates from a varactor-tuned, 10-crystal, oven-regulated, comb-source capable of continuously frequency-tuning a microwave oscillator anywhere within its range. With -3 dbm RF input power derived from a -20 db cross-guide dual-range coupler, optimum minimum residual noise and FM phase-lock sidebands were achieved at a modulation sensitivity of 3.0 MHz/V, as determined on a Tektronix Type 491 (narrow band) Spectrum Analyzer. Compared to a General Radio Model 1115-B C Frequency Standard with WWVB (atomic time) calibration traceability, the MOS-1 held the V-58 source to 6×10^{-10} parts (rms)/sec in a range environment and proved more than sufficient in correcting any deviation or frequency sensitivity due to temperature or reference path/signal path length disparity.

An E/H tuner following the source was used to lower the VSWR at the operating frequency to less than 1.1:1 looking into a broadband Narda Model 1210 isolator which provided at least 35 db isolation. Following the isolator and the dual range stabilization coupler mentioned above, another cross-guide coupler was used to power a coarse frequency monitor arm consisting of the following, a DeMornay Bonardi DBG-720 absorptive-mode nitrogen-filled precision cavity, a crystal detector and oscilloscope.

A precision attenuator and a four-port flap-switch follow the frequency monitor network. One arm of the switch feeds the signal/reference port while the other provides a cutoff mode and at the same

time permits the setting of power level and the monitoring of the output of the source. Power measurements are made using a HP X486A temperature-compensated balanced thermistor mount and an HP 431C Power Meter. Power variation at the fixed frequency setting provided by the MOS-1 stabilizer is virtually unmeasurable. The output of 0.5 watt was easily maintained over a long period with relatively infrequent adjustment required.

A Waveline Model 674 precision, high-directivity (-40 db) top-wall coupler was used to derive separate reference and transmission paths; the main guide contains the reference arm and the auxiliary guide (at -20 db, relative to the main arm), the signal or transmission arm. After suitable isolation with E & M X165 LIM miniature resonance absorption isolators, the two arms are routed their separate ways and these parts of the microwave circuit will be described individually.

2.3 Transmission Arms

Proceeding from one of the isolators just mentioned, along the signal arm, there is located a precision attenuator for setting the signal level transmitted through the horn/lens array. A power monitor plus the hybrid power divider were primarily all that preceded the dual antenna array. Calibration difficulties and ambiguities regarding polarity response necessitated a basic change in the mode of operation and they are the subjects of a small digression.

Since the interferometer operates throughout in a dc coupled mode, system drift becomes a large source of error when measured phase shifts down to 0.5 degrees are attempted. Further, small changes in the signal path due to changes in pressure (and therefore, dielectric constant) can cause a shift of the zero signal level. Frequency shift, although of a minor nature here due to frequency stabilization, can become another source of error. Lastly, and again a minor consideration, temperature should not be overlooked because of its effect on waveguide and components, especially phase shifters and attenuators.

Compounding the above errors is the problem of polarity of the displays. From a vector analysis of the SINE-COSINE outputs it is apparent that it is possible to derive functions which are 180 degrees out of phase with the display desired. As maximum gain factors are used in many of the recordings the ambiguity can easily lead to total loss of the oscilloscope trace.

The mechanical-switching on and off of the transmitted signal resolves part of the problem, but is laborious, slow, and it probably introduces more errors than it eliminates. It has therefore been found expedient to electrically chop or pulse the signal using a diode modulator with a large dynamic range. At first, the operation was restricted to a prefiring and/or post-firing procedure, allowing whatever errors due to drift during the firing cycle to go unmeasured. Subsequently, it was found that by a judicious choice of duty cycle, the transmitted signal could be gated off for short periods during a recording with negligible effect on system noise and phase resolution and so determine absolutely the dc base-line level and the polarity ambiguity.

To effect pulse modulation of the transmitted signal, an HP Model 8735B PIN Modulator with an 80 db dynamic range was inserted in the signal arm between the level set attenuator and the hybrid power splitter and driven with the correct waveshapes by an HP Model 8403A Modulator Driver. Because the design of the of 8403 did not permit internal operation beyond a 50% duty cycle, an external negative pulse from generated by an HP 214A Pulse Generator was provided, it in turn being externally triggered on by the master trigger in the Radiation Recording Room. The net effect gates the transmitted signal 'off' every 500 microseconds for a period not exceeding 50 microseconds permitting a relatively simple procedure for full-scale calibration deflection or zero setting of the SINE-COSINE displays and in addition providing a positive measure of system drift during the firing. This procedure will be detailed more fully under the description of the receiver and its method of calibration.

A 3 db hybrid power divider follows the modulator with each arm further isolated by E & M X165 LIM isolators. To effect positive electrical decoupling of the twin beams, one arm is physically rotated 90 degrees, effectively cross-polarizing the transmitted signals. A composite adjustable dual-channel, waveguide pressure-port provides a vacuum transition into the range (Fig. 6). Microwave Associates flange-mounted waveguide windows, Type MA1344, maintain range vacuum integrity at the ports. Conical horns terminate each port, illuminating the lens system and are described immediately below.

2.4 Horn-Lens Systems

The dual horn double lens focussing system (Fig. 5) used in the interferometer follows accepted design procedures (Ref. 9-12), and has been thoroughly investigated and reported elsewhere (Ref. 13). The choice of frequency was determined principally by the electron density range of interest, the latter having to be compatible with the range of densities capable of being measured with the other probe experiments. Other considerations such as those of desired resolution as related to model size, expected shot dispersion, safety factors, and range constraints can be partially influenced by design features including the determination of source-to-lens and lens-to-image distance, lens material and lens thickness.

Parameters relating to the defining of these factors in the horn-lens design are depicted in Figure 7. Although the lens and horn design are integrated parts of the focussing system, the lenses exert the greatest influence on the overall performance of the system and will be discussed first. Some of the preliminary designs considerations employed are discussed in Appendix A.

The choice of frequency of 9.60 GHz for the probing wave provides a realizable range of mean electron density measurements varying from 10^9 to 10^{12} electrons centimeter⁻³. The relationship of wake diameter to beam spot size is approached with the understanding that the beam be fully immersed in the wake as soon as possible after the passage of the

projectile so as to provide a fully integrated electron density value. Therefore, to accommodate early immersion and approximate more closely the well known uniform plane wave-cylindrical plasma interaction model (Ref. 9), a half power beam spot size of one half the wake diameter is desirable. For the 2.7 inch diameter spheres observed on Range 5, adequate resolution should be achieved with a -3 db beam width of $W = 1.35$ inches at an $X/D = 10$, at which distance the one-third law wake expansion/sphere diameter ratio reaches 1:1.

Range constraints limit the allowable transverse focussing system to something less than 10 feet. Assuming equality of the imaging system in terms of both magnification and refocussing, the source point and image point being at $L = 2f$, the maximum allowable separation becomes $f = 15$ inches.

The lens materials commercially available were subsequently narrowed to American Enka Brand Rexolite No 1422, a copolymer styrene. It possesses a reasonable index of refraction of $n = 1.59$ ($\kappa = 2.53$) and a loss tangent at the operating frequency of $\delta = 0.00066$, and at the same time is easily machinable. It can be bonded with adhesives possessing similar refractive indexes and has a reasonable density ratio.

Commercially available Rexolite No 1422 was limited to 3 X 24 X 24 inches blocks without special order so that fabrication of the lens proceeded in a double plano-convex configuration, with the figured surfaces derived from a computer program to provide the requisite hyperboloid. The finished diameter was set at $2a = 19.0$ inches with a thickness $t = 2.93$ inches. The focal length of the half lenses was set at $f = 24.0$ inches, the image point to lens surface distance. Each of the plano-convex lenses was fitted and cemented (adhesive was Rexolite No 12517) into a mounting disk of Rexolite No 1422 styrene 22.0 inches diameter and 0.75 inches thick and machine-recessed 0.1143 inches to hold the lens. The two half lenses were then pegged and cemented together to form a single composite double convex lens with a working diameter, $2a = 19.0$ inches, and overall thickness $t_1 = 7.16$ inches and a focal length of $f_1 = 12.0$ inches (Fig. 8). The F-number of the composite lens is $F_n = f/2a = f/d = 0.632$.

Two of these composite lenses form the focussing system of the interferometer, one on the TX side illuminating the wake and the other on the RX side to pick up and refocus the processed signals into the receiver horns (Fig. 5).

The horns selected for illuminating and receiving were chosen for a moderate degree of taper illumination (-4 db) of the lens, i.e., the ratio of I_e/I_a , or intensity of the edge illumination I_e to intensity of illumination on the axis I_a , varies at somewhat more than a $\frac{1}{2}$ power law. The configuration represents a compromise between transmission efficiency, minimum beam width, and maximum side lobe suppression (Ref. 12).

The cross-polarized dual conical horns were scaled up from existing 35 GHz models and fabricated from brass. Initially they were milled from solid interlocking blocks and formed an integral unit, but weight considerations imposed a mounting problem. Subsequently the conic sections were drill-formed with all excess material machined away. The conics were then fitted and brazed to standard WR-90 waveguide (Fig. 9).

While it was possible to site the antenna feed points (relative to the lens focussing axis) at any reasonable separation distance to achieve maximum spatial coverage (in the event of increased round dispersion), it was felt that the consequent degraded illumination patterns resulting from beam broadening and increased sidelobing due to off-axis spherical aberration, did not justify the effort involved. At the expense of reduced coverage, a compromise was implemented, the criteria being the minimum physical separation of the hybrid power divider and whatever horn flare angle was commensurate with an acceptable illumination taper. Given a hybrid guide separation of 1.625 inches, the allowable scaled flare-angle became 20 degrees for an overall flare length of 3.0 inches and a nominal equidistant horn spacing of 0.8125 inches (Fig. 10 and Appendix A). Nominal gain over isotropic was determined to be 10 db.

With a source distance of $L_1 = 2f$, the image focal point of the lens becomes $L_1 = L_2 = 24.0$ inches for an α factor = $L_2/f = 2$ which is the predetermined separation distance mentioned above. The normal optical inversion prevails with the upper and lower beams becoming reversed as to position at the range centerline. The second or refocussing lens merely reverses the process noting however, that detected signals must be interpreted as a consequence of the reversal, i.e., greater signal strength in the upper beam indicates a round fired low; the opposite obtains for rounds fired high (Fig. 10 and Appendix A).

As determined from a separate study of the field intensity pattern in the focal plane of the lens system (Ref. 13), an effective depth of field for the -3 db contour was found to be $D = 8.6$ inches and for the -10 db contour $D = 8.3$ inches. Conversely, a beam width for the -3 db contour was measured at $W = 2.0$ inches and for the -10 db contour $W = 3.2$ inches. For the -3 db contour, this gives a resolution of 0.74 of a sphere diameter which is somewhat more than the desired 0.50 or 1.35 inches referred to above. It should be noted from Figure 11 that the field intensity contours are not located symmetrically about the image point, but follow the expected $(\text{SIN } x/x)^2$ distribution of geometric optical theory with compression occurring in the -x space toward the lens (inside of focus) and expansion in the +x space away from the lens (outside of focus). Congruent with this asymmetry, is the location of the maximum intensity point derived from the expression $\delta I/\delta x = 0$, where I , is the field intensity and s , the distance from focus and occurs as shown, inside the image point (Fig. 12).

As previously noted, we have assumed that wake growth proceeds as a one-third law and reaches a 1:1 ratio with respect to projectile body diameter at an $X/D = 10$. (Additionally, it is assumed for analytical purposes, that the standard electron distribution exhibits a gaussian form through the wake). Using the above parameters, we can conclude that total beam immersion occurs near an $X/D = 8$ for the -3 db contour for rounds fired on either beam axis and that the desired resolution of 0.5 for beam width to wake diameter ratio is achieved at an $X/D = 15$.

The plotted deviation from the range axis of 2.7 inch sphere rounds fired on the Range 5 facility is not more than 3.0 inches at the butt (450 feet) with a confidence of 95%. At the interferometer station (272 feet), the dispersion factor is 0.6 (1.8 inches) which at the computed wake growth would complete beam immersion at an $X/D = 15$. For the resolution factor to apply, this X/D value would have to be doubled.

For rounds displaced laterally in the beam axis, the -3 db depth of field contour with $\pm 5\%$ deviation from nominal will provide a constant illumination up to 3 diameters (8.6 inches) and preferably biased toward the TX side without, however, entering the disturbed field near the lens. This $\pm 5\%$ (10% total) permissible variation in the field intensity of the zone as applied by Carswell and Richard, would appear to be overly restrictive from an engineering standpoint (Ref. 12, 13). If the permissible variation is increased to $\pm 10\%$ (20% total), the depth of field expands to 5 diameters (12.0 inches) which appears adequate at least, in measuring wake densities up to 400 diameters (Fig. 13).

The refocussing lens optically reverses the transmitted signals and focusses the microwave energy into another set of conical horn antennas physically identical to those of the TX. They are similarly mounted and pressure sealed on their own pressure plate (Fig. 14). Using the standard detector system with amplification, cross-talk between the cross-polarized channels was virtually unmeasurable and may be disregarded. Detected receiver power at the individual horns was measured at values ranging from $P_r = 12$ to 24 microwatt for transmitted powers of $P_t = 350$ to 700 microwatt, the resultant transmission losses being on the order of 14.7 db.

To prevent unwanted sidelobe or primary edge diffraction effects, surfaces near or facing the TX were covered with Emerson and Cumings AN-73 (-20 db) sheet absorber and in more critical areas, E & C CV-4 (-40 db) electrically tapered (waffle) absorber (Fig. 5).

2.5 The Receiver System

The receiver and detector system of the interferometer is depicted in a general way in Figure 3. Together with the requisite reference signal network, they provide a standard dual-channel SINE-COSINE recording capability. Following the antenna pressure transition, each input is isolated with E & M X165 LIM isolators to prevent cross-coupling and other stray return reflections from influencing the signals produced

by interaction with the wake plasma. Highly directive Waveline 3 db topwall couplers were employed to divide each channel into SINE and COSINE arms. E & M miniature transverse-field SM-76 isolators further isolate both the signal and the reference input arms of the four MDL short-slot hybrid single-ended mixers; the unused port is terminated in a matched load.

The reference signal arm passing under the range via WR-90 rectangular guide is first modified by an HP X885A precision rotary phase shifter acting as a primary phase control and ultimately is routed through a divider network where it is split twice into four isolated arms. Each arm possessing its own HP X382A precision rotary attenuator and HP X885A rotary phase shifter, is joined to its own hybrid mixer as described above. Reference signal power levels usually impressed on the crystal detectors vary around a ratio of 100:1 with respect to signal power and do not exceed 3.0 milliwatt, the nominal level being 500 microwatt.

2.6 Detection and Amplification Network

The mixed reference and transmitted signals operating at power level ratios of 100:1 drive matched MA-611 octave-band low noise crystal detectors incorporating quad-matched IN-23G crystals. The crystals operating into low noise 10 kilohm video loads, are driven, autodyne mode, into the middle of their respective linear response curves by the large reference signals. The video loads comprise part of the input networks of four Tektronix Type 'O' operational plug-ins acting as summation network amplifiers with a bandwidth from dc to 100 kHz. (max). Typical crystal response curves are shown in Figure 15.

Internally derived negative voltages, after current limiting, are fed to resistive voltage dividers incorporating 10-turn helipot for fine setting of the dc differential comparator voltages. Summation resistors complete the input to the single-stage amplifiers where cancellation of the large dc component due to the reference signal is effected. Single stage X10 amplification and polarity inversion complete this network.

The outputs of the 'O' units drive HP 467A amplifier/line-drivers which are set at an additional X10 gain for a total amplification factor of X100. The four 93 ohm signal lines are terminated in their characteristic impedance at a 5 watt level some 250 feet distant in the Radiation Recording Room of Range 5.

2.7 Recording

Signals are displayed on Tektronix Type 555 or 550 oscilloscopes usually in pairs, i.e., twin SINE and twin COSINE signals. A total of five oscilloscopes are usually employed with gains varying from 5 to 100 centimeter full scale deflection for 90 degrees of phase shift. Sweep delay and deflection rate are also varied to effect the greatest possible dynamic range and resolution. Recordings are normally made on Polaroid cameras although a few rounds have been run using 35 millimeter Fastax high-speed cameras (Fig. 16).

3.0 CALIBRATION PROCEDURE

The round-to-round calibration of the X_S-Band interferometer on Range 5 is a reasonably straightforward operation and is described briefly in the following paragraphs.

Pumpdown of the range tank usually occupies approximately 2 hours with the interferometer being activated about half way through this cycle. After the range tank has been evacuated to its lowest level (≈ 0.1 torr) and the electronics have stabilized, all the phase shifters in the four reference arms of the interferometer are coarse-set to produce a SINE (or null) display at the signal outputs of the line drivers as measured on the small calibration oscilloscope set to low gain and ac coupled. Then, switching to dc coupling and still at a low gain setting, the -dc comparator voltages are sequentially adjusted to approximately cancel the large +dc reference components in the signals with the SINE 'off' and COSINE 'on' sections of the waveforms set to the dc baselines respectively. After recording the readings of the four phase shifters, they are rotated 90 degrees in a CW direction for a maximum (COSINE) deflection display. An expansion of the SINE displays in a positive direction will be obtained if the phase shifters have been located in their correct quadrants. If not, negative going waveforms will result and, following normal recording procedures, with the SINE baselines sited negatively and the COSINE baseline positively on the recording oscilloscope screens, the response curves will be reversed and the traces will be either cross-recorded or totally lost off-screen.

After positively determining the correct phase responses, the four reference attenuators are individually adjusted for maximum excursion of the chopped TX 'on-off' waveforms. It should be noted here that the maximum excursion referred to does not indicate saturation or limiting on the part of the crystal detectors or the amplifier chains. The outputs are strictly limited in a dynamic sense by the available input signals (at values ≤ 10 microwatts) plus the reference bias voltage (≤ 3.0 milliwatts) and do not in any case exceed the capabilities of the system. Maximum excursion of the waveforms' positive and negative peaks indicates therefore a positive bias level midway in the diode detection curves, the response being linearly proportional to input. Further increases in the reference drive will result in compression of the waveforms and 'is' indicative of saturation of the diode detectors.

Alternating between SINE and COSINE displays at high vertical amplifier settings on the calibration oscilloscope, the four channels are progressively fine-set and balanced to zero dc settings throughout all the detection and amplification strings. Then, the channels are set in positive COSINE mode and the dc coupled recording oscilloscopes are adjusted using their vertical amplifier turret and vernier attenuator controls to produce a full scale 'on-screen' deflection of the requisite magnitude. Finally, to produce the desired gain factors, the vertical attenuator turret controls are rotated in steps to produce the full scale 'off-screen' overall gain,

being careful however, to avoid displacing the vertical vernier control. With the display running up to 100 centimeters FSD, only the TX 'off' condition (50 microseconds) of the SINE display and the TX 'on' (450 microseconds) condition of the COSINE display are viewed on the zero dc baseline. They are set, at this stage, to their respective dc offsets on the oscilloscopes.

After the above calibration is completed, the phase shifters are returned CCW to their SINE (null) position and together with the -dc comparator voltages are maintained at zero dc settings until 15 minutes prior to firing at which time, the vertical calibration is again checked to correct any errors due to drift.

Final phase null positions are determined at the point range gas (N_2 or air) is loaded and the range tank has reached equilibrium. Little if any adjustment is necessary if range pressure does not exceed 10 torr. Beyond this pressure, a small amount of correction, usually < 0.7 degrees for $P_\infty = 20$ torr, is necessary and may be preset into the phase shifters from established line graphs.

Final settings, if required, are made approximately 4 minutes before firing with the SINE channels set to their respective nulls and the COSINE channels arbitrarily offset 90 degrees CW from their respective null settings. dc baselines are set terminally, approximately 3 minutes before firing after which cameras are closed and oscilloscopes set to single sweep. Shutters are actuated and oscilloscopes armed at T minus 10 seconds, with automatic sequencing in control of the actual firing cycle. Polaroid prints are available within a minute subsequent to completion of firing.

Some system noise and stability problems associated with phase-lock FM noise and the -dc comparator network originally installed limited the degree of resolution attainable with the interferometer. A more judicious choice in the selection of the klystron reflector phase-lock feedback network and more critical attention to phase-lock fine tuning resolved the former difficulty. Incorporation of the summation and -dc comparator networks within the preamplifier 'O' units (with a commensurate reduction in lead capacitance) greatly reduced the latter. Attenuator switching boxes were originally installed on the recording oscilloscopes as a means of controlling the gain factors in recording. These were dropped subsequently when it was found they contributed little to the smooth operation of the system and tended to introduce unwanted capacitive effects, probably some mismatch, and could not, in any case, exceed the accuracy attainable in the turret attenuators of the oscilloscopes.

4.0 ANALYSIS

4.1 Determination of Transmission Arm Phase Shifts

As indicated previously, the detector crystals are biased by means of the reference signal to the appropriate current level for operation as linear detectors. Under these conditions, the detector current is proportional to the field strength in the guide.

$$\Delta I_d \sim K_d \Delta V_q$$

The voltage at the output of the hybrid mixer and incident upon the detector consists of the vector sum of the reference arm signal and the transmission arm signal

$$\vec{V} = \vec{V}_r + \vec{V}_s$$

In operation, the reference signal \vec{V}_r , is made at least 2 orders of magnitude greater than the transmission arm signal \vec{V}_s . The situation is represented in Figure 17.

Let A represent $|\vec{V}_s|$ and B represent $|\vec{V}_r|$ and let ϕ be the phase angle between \vec{V}_r and \vec{V}_s . Then the resultant field at the detector has the magnitude

$$\begin{aligned} |\vec{V}| &= ((B+A \cos\phi)^2 + (A \sin\phi)^2)^{1/2} \\ &\approx B + A \cos\phi. \end{aligned}$$

Suppose further, that in the absence of any plasma (or electrons) in the transmission arm, that we align \vec{V}_r and \vec{V}_s so that $\phi_0=0$. Then let the phase shift due to the introduction of a plasma in the transmission arm be

$$\begin{aligned} |\vec{V}|_{\Delta\phi} &= B + A \cos\Delta\phi \\ |\vec{V}|_{\phi_0=0} &= B + A_0 \end{aligned} \tag{COSINE}$$

In the last equation we have distinguished between the amplitude A_0 of the reference arm signal \vec{V}_s in the absence of a plasma ($\Delta\phi=0$) and the amplitude A in the presence of plasma and phase shift (non-zero $\Delta\phi$). (At high electron density levels and high pressures the signal transmitted across the plasma may undergo attenuation as well as phase shift so that $A < A_0$. However, for the conditions encountered in the present experiment $A = A_0$).

The difference in voltage due to the addition of the phase shift is consequently

$$\Delta |\vec{V}|_{\Delta\phi_c} = A \cos\Delta\phi - A_o \quad (\text{COSINE})$$

and the change in diode current

$$\Delta I_{d\Delta\phi_c} = K_d (A \cos\Delta\phi - A_o). \quad (\text{COSINE})$$

For low pressure weakly ionized plasmas such as encountered in the present work, $A = A_o$ and

$$\Delta I_{d\Delta\phi_c} = K_d A_o (\cos\Delta\phi - 1) \quad (\text{COSINE})$$

We shall call this particular type of detection as COSINE detection (Figure 18).

If instead of choosing $\phi = 0$ we had chosen $\phi_o = \frac{\pi}{2}$ we would have had

$$|\vec{V}|_{\Delta\phi} = B + A \cos\left(\frac{\pi}{2} + \Delta\phi\right) \quad (\text{SINE})$$

$$|\vec{V}|_{\phi_o = \frac{\pi}{2}} = B$$

and

$$\Delta |\vec{V}|_{\Delta\phi_s} = -A \sin\Delta\phi \quad (\text{SINE})$$

and

$$\Delta I_{d\Delta\phi_s} = -K_d A \sin\Delta\phi \quad (\text{SINE})$$

For low pressure weakly ionized plasmas, we replace A by A_o

$$\Delta I_{d\Delta\phi_s} = -K_d A_o \sin\Delta\phi \quad (\text{SINE})$$

which will be referred to as SINE detection (Figure 19).

An important point becomes obvious by comparing the small phase shift case for the two types of detection:

$$\text{COSINE: } \Delta I_{d\Delta\phi_c} = -K_d A_o \frac{\Delta\phi^2}{2}$$

$$\text{SINE: } \Delta I_{d\Delta\phi_s} = -K_d A_o \Delta\phi.$$

Obviously for small phase shift it is better to operate with SINE detection.

(It should be obvious that the negative signs here can easily be altered to plus signs by the introduction of 180 degrees phase changes and are not important to this discussion).

For situations where high electron density levels are encountered or where attenuation as well as phase shift occurs in the transmission arm, both SINE and COSINE detection are required. Each detector arm is so arranged as to incorporate simultaneously both type of detection so that we have for the i_{th} channel

$$\Delta I(i)_{d\Delta\phi_c} = K_d(i,c) A(i) \text{COS}\Delta\phi(i) - K_d(i,c)A_o(i)$$

$$\Delta I(i)_{d\Delta\phi_c} = K_d(i,s) A(i) \text{SIN}\Delta\phi(i),$$

where i , refers to channel 1 or channel 2.

The two measurements ($i = 1,2$) enable us to solve for the two unknowns $A(i)$ and $\Delta\phi(i)$.

In the method of recording on the DREV Range 5 interferometer, the signals are recorded from oscilloscopes using Polaroid cameras. The deflection sensitivities of the oscilloscopes are established first prior to the firing by chopping the energy in the transmission arm and calibrating the sensitivity setting in terms of the amplitude A_o of the electric field in the transmission arm in the absence of any plasma. The calibration is done in the COSINE arms after ensuring $\phi_o = 0$ and in the SINE arms by removing $\frac{\pi}{2}$ radians from the value of $\phi_o = \frac{\pi}{2}$ in these arms during the calibration period. Essentially the oscilloscopes are adjusted so that a deflection on the oscilloscope screen of 5, 10, 20 or 40 centimeters represents the amplitude A_o . The procedure is fully described in Section 3.0.

4.2 Characteristics of Wake Electron Density Distribution

According to analyses which may be found in standard texts (Ref. 10), the phase shift, arising along the path of a plane wave when an electron density function $n(x)$ is introduced instead of free space, is given by

$$\begin{aligned} \Delta\phi &= \int_{\text{path}} \left(1 - \left(1 - \frac{n(x)}{n_c}\right)^{\frac{1}{2}}\right) \frac{2\pi}{\lambda} dx \\ &\approx \frac{\pi}{\lambda} \frac{1}{n_c} \int n(x) dx, \end{aligned}$$

provided that $\frac{n(x)}{n_c}$ is always less than unity. The so-called critical electron density n_c , is given by

$$n_c = \frac{\epsilon_o m \omega^2}{e^2}$$

where ω is the microwave angular frequency
 ϵ_0 is the permittivity of free space
 m is the electron mass
 e is the electron charge

Substituting

$$\begin{aligned}\Delta\phi &= \frac{e^2}{2\epsilon_0 mc\omega} \int_{\text{path}} n(x) dx \\ &= \frac{1}{\omega} \frac{2\pi}{118.4} \int_{\text{path}} n(x) dx\end{aligned}$$

where x is measured in centimeters and $n(x)$ in centimeter⁻³

Two one-dimensional distributions of $n(x)$ are of interest:

- 1) For the one-dimensional slab of width L and constant electron density n_0

$$\begin{aligned}n(x) &= n_0, \quad -\frac{L}{2} < x < \frac{L}{2} \\ &= 0, \quad |x| > \frac{L}{2}\end{aligned}$$

$$\int n(x) dx = n_0 L.$$

- 2) For a one-dimensional state having a gaussian distribution of electron density

$$n(x) = n_0 e^{-x^2/L^2}, \quad 0 < |x| < \infty$$

$$\int n(x) dx = \sqrt{\pi} n_0 L.$$

However, for purposes of estimating electron density in the more or less cylindrical wake, we are interested in assuming that the appropriate distribution is gaussian in cylindrical coordinates

$$n(r) = n_0 e^{-r^2/R^2}, \quad 0 < r < \infty.$$

Then, assuming a microwave beam passes through this distribution at a distance y from the center (Figure 20), we have that

$$n(x) = n_0 e^{-y^2/R^2} e^{-x^2/R^2}$$

and

$$\int n(x) dx = \sqrt{\pi} n_0 \text{Re}^{-y^2/R^2}.$$

Suppose now that we have two focussed microwave beams looking at a cylindrical plasma (as is the case with the DREV Range 5 interferometer system) and suppose that the plasma has a gaussian distribution of electron charge $n(r) = n_0 e^{-r^2/R^2}$. Then if one beam traverses the cylinder at an offset distance from the axis of y_1 and the second beam traverses at an offset distance y_2 , then the two phase shifts occurring in the beams will be respectively

$$\Delta\phi_1 = K \sqrt{\pi} n_0 \text{Re}^{-y_1^2/R^2}$$

and
$$\Delta\phi_2 = K \sqrt{\pi} n_0 \text{Re}^{-y_2^2/R^2},$$

where
$$K = \frac{1}{\omega} \frac{2\pi}{118.4}.$$

The two parameters of the gaussian distribution of electron density n_0 and R , may be determined by solving these two equations in terms of the measured phase changes $\Delta\phi_1$ and $\Delta\phi_2$ and the known offset distances y_1 and y_2 .

Consequently

$$R^2 = (y_2^2 - y_1^2) \log_e (\Delta\phi_1/\Delta\phi_2)$$

determines R , and subsequently

$$n_0 = \frac{\Delta\phi_j}{KR \sqrt{\pi}} e^{-y_j^2/R^2}$$

for $j = 1$ or 2 .

Insofar as a gaussian distribution is appropriate for describing the electron density in the wake, a two-channel interferometer offers the possibility of determining the amplitude n_0 and width R of the distribution.

5.0 RESULTS

5.1 Typical Data

Data are normally recorded at high sweep speed (200 ms/cm) low sensitivity (maximum deflection 5 cm) and at relatively lower sweep speeds (0.5 and 1.0 ms/cm) and higher sensitivities (maximum deflection 10 cm and 20 cm) in order to ensure the capture of all parts of the signal at more or less optimum recording conditions. Except for 'dirty' rounds, so-called because of random observations on dirty atmospheres or damaged projectiles, it soon became apparent that there was very little signal on the COSINE channels and the recording of these were subsequently dropped. The amplitude of the transmitted signal was assumed to remain constant, and all the signal change observed in the SINE channels was attributed to phase shift. Figure 21 shows a typical data Round Sheet recording details of a firing observed with the interferometer equipment. Examples of the signals recorded on polaroid films are shown in Figure 22. In this particular round, phase shifts of up to 44 degrees were observed during the first 200 microseconds; after 9 milliseconds had elapsed, the detected phase shift has shrunk to about 0.5 degree. With care, the interferometer system can measure phase changes to an accuracy slightly better than 0.5 degree.

Figure 23 shows the amplitude of the electron density distribution along the wake axis N_0 , while Figure 24 shows the radius of the gaussian profile assumed to describe the distribution of the electron density. On these two figures, the open circles denote data from the polaroid recorded at 5 centimeter sensitivity and 0.2 millisecond/centimeter sweep, the diamonds denote data recorded at 0.5 millisecond/centimeter sweep and 20 centimeter sensitivities, while the open squares were recorded at 1.0 millisecond/centimeter sweep and 20 centimeter sensitivity. Normally the data recorded at the higher sensitivity should be more accurate, except at very large axial distances, where the signal/noise ratio becomes overly degraded and increased sensitivity does not help.

From Figure 23, it will be seen that the decay of the electron density can be followed from about 10^{11} to less than 10^9 electrons centimeter⁻³ with this technique, from just behind the projectile to about 200 diameters. At larger values of X/D , the results scatter badly. The behavior of the electron density radius of the wake as shown in Figure 24 is interesting because of the indication of the smallness of this radius compared to other commonly defined wake radii.

Figure 25 shows a comparison of data obtained on about 3 selected rounds. The rounds were selected on the basis of being supposedly clean. Thus Figure 25 gives some idea of the reproducibility of the results under nominally 'clean' firing conditions.

5.2 Comparison with Outside Ballistic Range Data

The largest amount of ionization data available in the open literature appears to be that obtained by Defence Research Laboratories (GM ACDRL) (Ref. 7). In the case of interferometer results, their data is obtained with a fence of detectors. Using the phase shifts measured by each channel, the phase shift at the center of the wake is interpolated. However, in contrast to the analysis technique used at DREV, the GM ACDRL results are reported as a line integral of charge density through the wake center, or an equivalent $\overline{Ne D_p}$, where \overline{Ne} is an average electron density and D_p the diameter of the plasma.

MIT Lincoln Laboratory (Ref. 8) has also published electron density data. However, their data is in the form of a volume integral (per unit length).

5.2.1 Transformation of GM ACDRL Data

In order to compare with GM ACDRL data, we wish to compute an equivalent $\overline{Ne D_p}$ from the DREV results, using the deduced electron density on the wake axis N_0 and the deduced wake electron density radius r_n/D . Both N_0 and r_n are functions of axial distances.

Then for a line integral of electron density passing through the wake axis we have

$$\int_{D_p} Ne dr = \int_{-\frac{D_p}{2}}^{+\frac{D_p}{2}} N_0 e^{-r^2/r_n^2} dr.$$

If we identify $D_p = 2r_n$ we compute

$$\int_{D_p} Ne dr = 1.49 N_0 r_n.$$

However, if we identify $D_p = 4r_n$, we compute

$$\int_{D_p} Ne dr = 1.77 N_0 r_n.$$

For comparison purposes, then, we will identify an equivalent $(\overline{Ne D_p})_{DREV}$ where $(\overline{Ne D_p})_{DREV} = 1.5 N_0 r_n$.

Finally in order to non-dimensionalize the comparison and thereby remove the effect of sphere size we will normalize both GM ACDRL and DREV results by the sphere diameter.

Thus we will compare

$$\left(\frac{\overline{Ne Dp}}{D}\right)_{\text{GM ACDRL}} \text{ and } \left(1.5 No \frac{r_n}{D}\right)_{\text{DREV}}$$

5.2.2. Transformation of MIT Lincoln Laboratory Data

In this case we wish to compute an equivalent $\int Ne d vol$ from the DREV results and compare this with line density measurements of Kornegay (Ref. 8).

$$\begin{aligned} \int_{Vol} Ne d vol &= \int_{-\infty}^{\infty} No e^{-r^2/r_n^2} 2\pi r dr, \\ &= \pi r_n^2 No \end{aligned}$$

where No and r_n/D are the parameters of the gaussian distribution of electron density assumed for the analysis of the interferometer results at DREV.

(For comparison purposes we will identify an equivalent line density $(N \text{ tot})_{\text{DREV}}$ where

$$(N \text{ tot})_{\text{DREV}} = \pi r_n^2 No$$

To remove the effects of different projectile size we will normalize by the square of the sphere diameter D

Thus we will compare

$$\left(\frac{N \text{ tot}}{D^2}\right)_{\text{DREV}} \text{ and } \left(\pi No \frac{r_n^2}{D^2}\right)_{\text{DREV}}$$

5.2.3 Comparison with Theoretical Calculations of AVCO

Sutton has made calculations of the average electron density in the wake of 2.7 inch diameter spheres launched in air atmospheres at 10 torr and 20 torr air. The average electron density \bar{n}_e is the cross section average of the inviscid electron density up to the turbulent front^{1/3}. The turbulent front radius used by Sutton corresponds to $y_f/D = 0.44 (X/D)^{1/3}$.

To compute the total electron density N_{total} , we have multiplied the mean value \bar{n}_e calculated by Sutton by the volume of the wake based on the front radius, here represented by $r/D = 0.4 (X/D)^{1/3}$ as determined by DREV measurements

$$N_{total} = \bar{n}_e \pi r^2$$

or

$$\begin{aligned} \frac{N_{total}}{D^2} &= \bar{n}_e \pi \frac{r^2}{D^2} \\ &= \bar{n}_e \pi (0.16 \frac{X^{2/3}}{D^{2/3}}) \\ &= 0.5 \bar{n}_e (X/D)^{2/3} \end{aligned}$$

Thus using the results of section 5.2.2, we should compare $(\pi \text{ No } \frac{r^2}{D^2})_{DREV}$ and $(0.5 \bar{n}_e (X/D)^{2/3})_{SUTTON}$.

5.2.4 Results of Comparison of Data

Figure 26 compares interferometer measurements obtained at GM ACDRL (Ref. 9) and DREV, the DREV data having been put in a form equivalent to that of the GM ACDRL data (Sec. 5.2.1). The difference of order of a factor of 10 can probably be explained as mainly due to the difference of about 1400 feet/second in velocity. (The $P_{\infty}D$ of the DREV data is 54 torr inches compared to 30 torr inches for the GM ACDRL data).

Figure 27 attempts to compare DREV interferometer data at 14.5 kilofeet/second with MIT Lincoln Laboratory data at 18 kilofeet/second or more and succeeds mainly in showing data obtained at such widely different conditions are not comparable. The calculated data from Sutton (Ref. 4) are however in good agreement with the DREV data.

6.0 CONCLUSION

The requirement for a microwave interferometer to make measurements of the mean electron density in the wake of hypersonic projectiles has been indicated on the basis of a program of experimental investigation of turbulent wake properties using Langmuir probes and ion probes. Details of the dual channel focussed beam X_s-Band interferometric equipment constructed and installed on Range 5 have been given, with particular attention to the horn-lens systems, the transmitter and receiver systems, the calibration procedures and the analysis of the results. The analysis technique employed uses the measurements made in the two channels

to determine the amplitude and width of the assumed gaussian distribution of electron density in the wake. Typical results show that for a 2.7 inch diameter sphere launched at 14,600 feet/second in 10 torr air, the electron density decays from about 10^{11} centimeter⁻³ just behind the projectile to less than 10^9 centimeter⁻³ at about 200 diameters behind the projectile. The electron radius of the wake is found to be small. It is shown how to recast the DREV measurements into a form which permits comparison with integrated electron density measurements obtained at GM ACDRL and at MIT Lincoln Laboratory. A good comparison of the DREV results with these other data is not possible because the conditions of projectile size, velocity and pressure vary too widely.

7.0 ACKNOWLEDGEMENTS

The authors acknowledge with gratitude the support, and able assistance of the many DREV personnel involved in the successful completion of this project. They include Dr. A. Lemay, former Director of Aerophysics Division, D. Audet, N. Bérubé, F. Devereux, M. Doutre, P. Doyon, A. Emond, G. Gobeil, P. Guay, G. Moisan, A. Perreault, C. Proulx, L. Sévigny, P. Solnoky, L. Tardif and J. Williams. The manuscript was prepared by Mrs C. Bigras.

UNCLASSIFIED

22

REFERENCES

1. Heckman, D., Tardif, L. and Lahaye, C., "Experimental Study of Turbulent Wakes in the CARDE Free-Flight Range", Proc. of the Symposium on Turbulence of Fluids and Plasmas, Vol. 18, Polytechnic Press of the Polytechnic Institute of Brooklyn, N.Y., 1968.
2. Lahaye, C., Léger, E., Dufresne, M., Doyle, H. and Boucher, P., "The Sequential Spark Technique: A Tool for Wake Velocity Studies in Ballistic Ranges", ICIASF'71 Record of the 4th International Congress on Instrumentation in Aerospace Simulation Facilities, pp. 33-44, June 1971.
3. Ellington, D., Park, K. and Desjardins, P., "Hypersonic Wake Studies Using Cooled-Film Anemometer Techniques", ICIASF'71 Record of the 4th International Congress on Instrumentation in Aerospace Simulation Facilities, pp. 45-59, June 1971.
4. Heckman, D., Emond, A., Fitchett, A. and Sévigny, L., "Mean and Fluctuating Charge Density Measurements in Turbulent Hypersonic Sphere Wakes", ICIASF'71 Record of the 4th International Congress on Instrumentation in Aerospace Simulation Facilities, pp. 68-79, June 1971.
5. Dionne, J.G.G. and Tardif, L., "An Application of the Electron Beam Fluorescence Probe in Hyperballistic Range Wake Studies", ICIASF'71 Record of the 4th International Congress on Instrumentation in Aerospace Simulation Facilities, pp. 80-86, June 1971.
6. Cantin, A., Emond, A. and Heckman, D., "Observations on Electrostatic Probe Behavior in Collision-Dominated Ionized Turbulent Gas Flows in Ballistic Ranges", ICIASF'69 Record of the 3rd International Congress on Instrumentation in Aerospace Simulation Facilities, pp. 20-23, May 1969.
7. Hayami, R. and Primach, R., "Integrated Electron Density in the Near Wakes of Hypersonic Velocity Spheres", GM Defence Research Laboratories, TR64-01F, May 1965. Unclassified.
8. Kornegay, M., "Electron Density Decay in Wakes", AIAA Journal, Vol. 3, No. 19, pp. 1819-1823, October 1965.
9. Hayami, R. and Primach, R., "Wake Electron Density Measurements Behind Hypersonic Spheres and Cones", Advisory Group for Aerospace Research & Development (AGARD), AGARD Conference Proc. No. 19 (Preprint), Fluid Physics of Hypersonic Wakes, May 1967.

10. Heald, M. and Wharton, C., "Plasma Diagnostics with Microwaves", John Wiley and Sons, 1965.
11. Kock, W., "Instrumentation, Calibration, and Data Reduction Methods", GM DRL TR 62-213, pp. 11-28, December 1962. Unclassified.
12. Carswell, A. and Richard, C., "Focal Properties of Microwave Lenses with Small F-Numbers", Applied Optics, Vol. 10, No. 2, pp. 346-357, February 1971.
13. Fitchett, A., "Resolution of the Microwave Lens System Used in an X_s-Band Interferometer", DREV TN 1998/72 (Unclassified).
14. Heckman, D., Lahaye, C., Moir, L., Podesto, B. and Robertson, W., "A Shock Wave Attenuation Treatment for Ballistic Ranges", AIAA Journal, Vol. 1, No. 7, pp. 1355-1357, July 1970.
15. Silver, S., "Microwave Antenna Theory and Design", McGraw-Hill, 1949.
16. Bitzer, R. and Holt, E., "A Microwave Lens System for Plasma Diagnostics", NASA CR-319, October 1965. Unclassified.

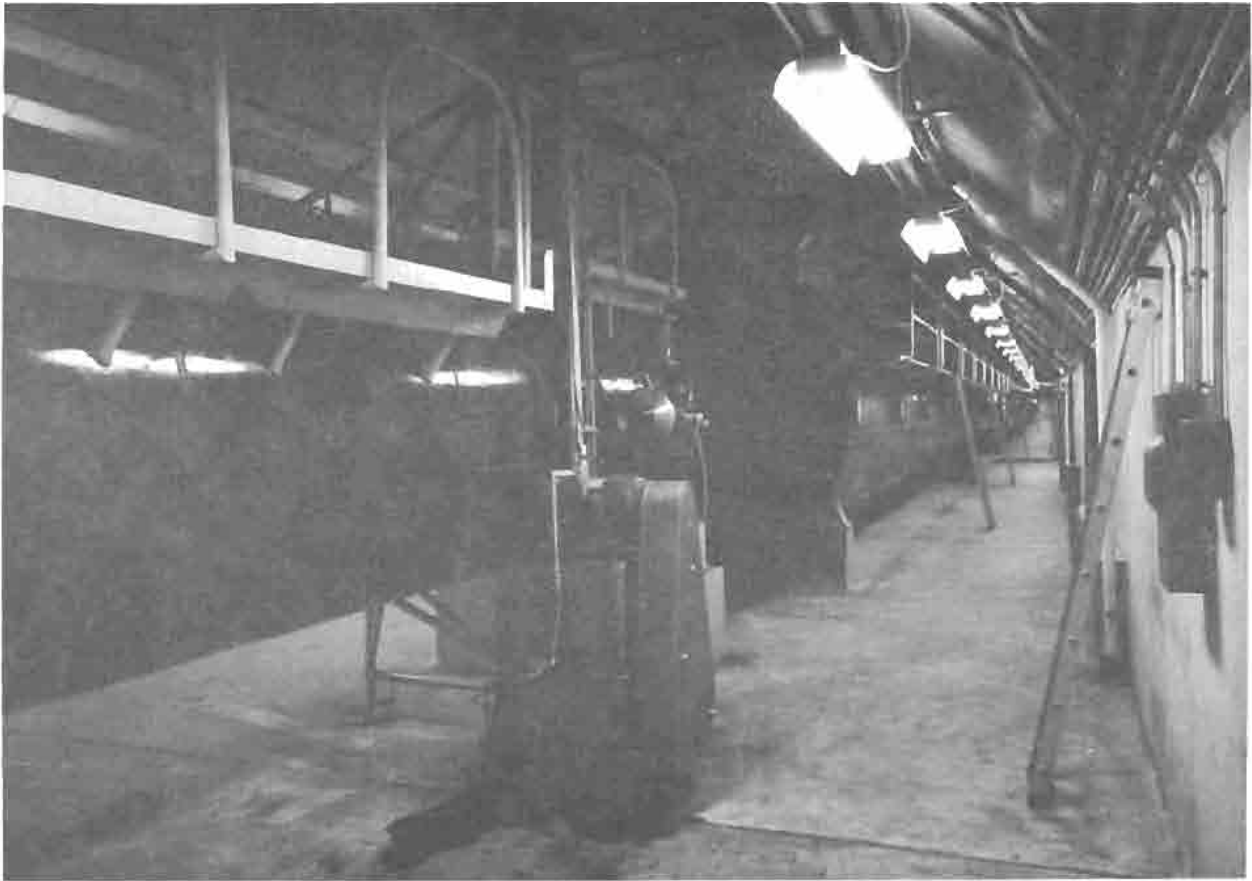


Fig. 1 View of the exterior of the Range 5 Flight Tank.

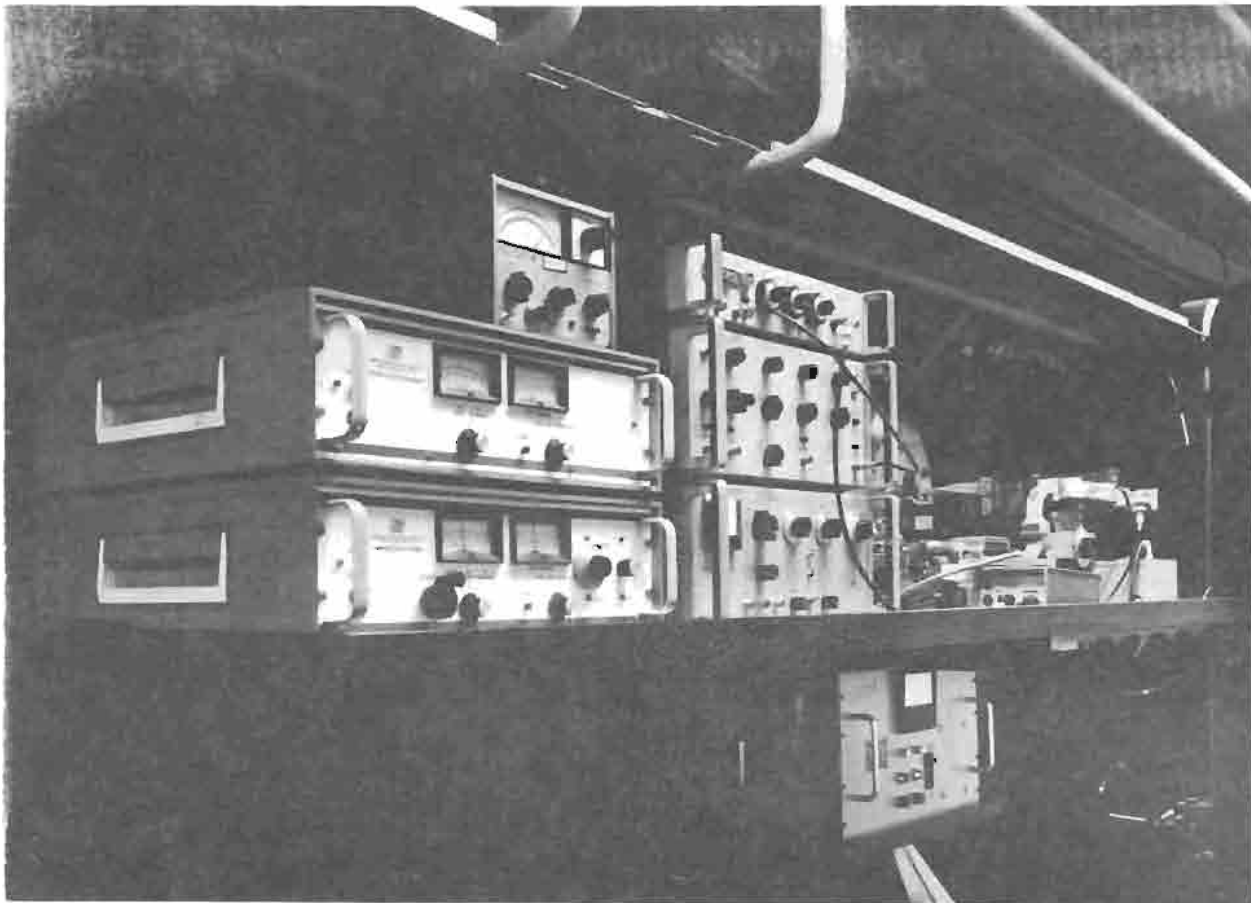


Fig. 2 Equipment bay at the Interferometric Station 272 (North Side).
From the top:

- Left - Power meter 431C, Slave Synchronizer PLS-(X) 60 (not used), Primary Synchronizer MOS-1
- Center - Pin Modulator Driver 8403A, Pulse Inverter Driver 214A, Klystron Power Supply 716B.
- Right - X_S -Band Klystron and associated signal and reference waveguide and hardware.

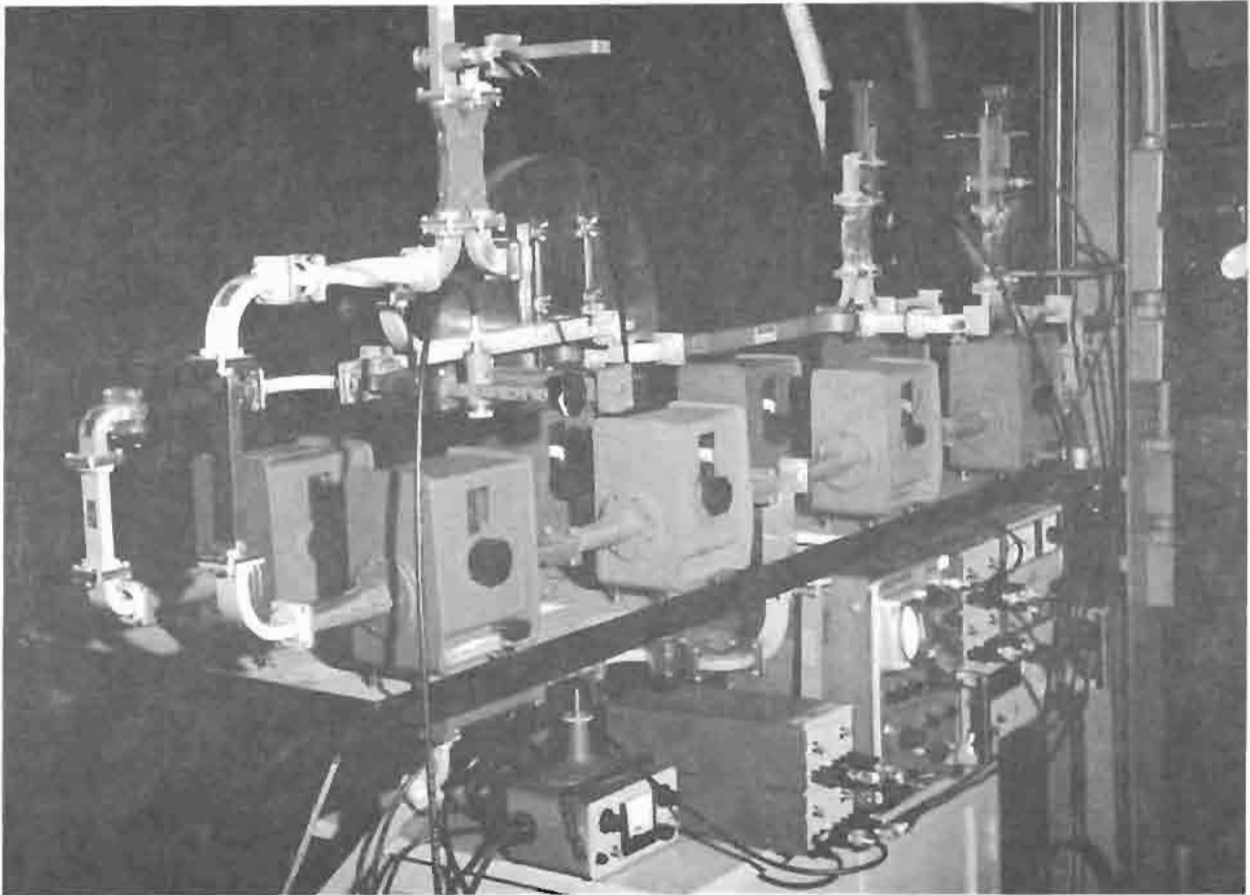


Fig. 3 Equipment bay at the Interferometric Station 272 (South Side). The reference and transmitter signals are mixed and detected in the short-slot side-wall hybrid couplers shown at the top of the photograph. The rectangular boxes in the lower part of the photograph contain the precision rotary phase shifters and attenuators.

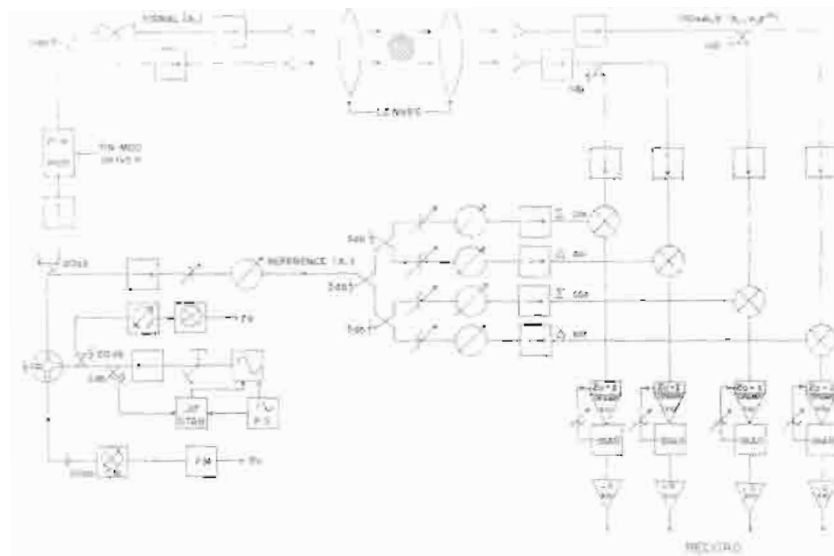


Fig. 4. Block diagram of the X_s-Band Microwave Interferometer. Transmitter section, lower left; Modulator, Upper left; Horn-Lens systems, upper center; Receiver section, right.

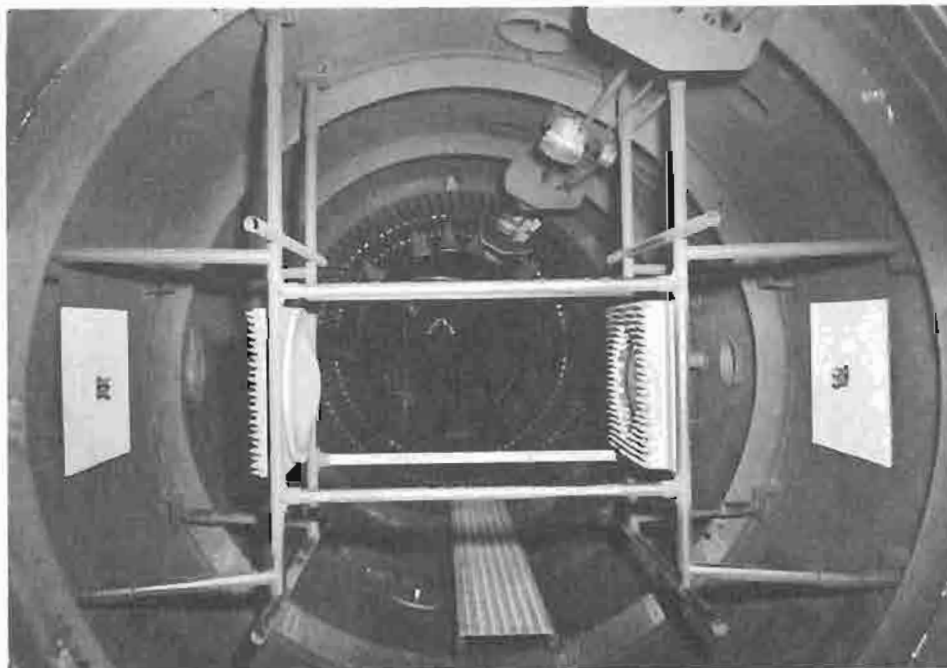


Fig. 5. Wide-angle photograph of the range interior at the Interferometric Station 272 showing transmitter antenna (left) the double focussing lens system (center), and the receiving antenna (right). The focussing lens (right) is partially obscured by E & C CV-4 microwave absorber.

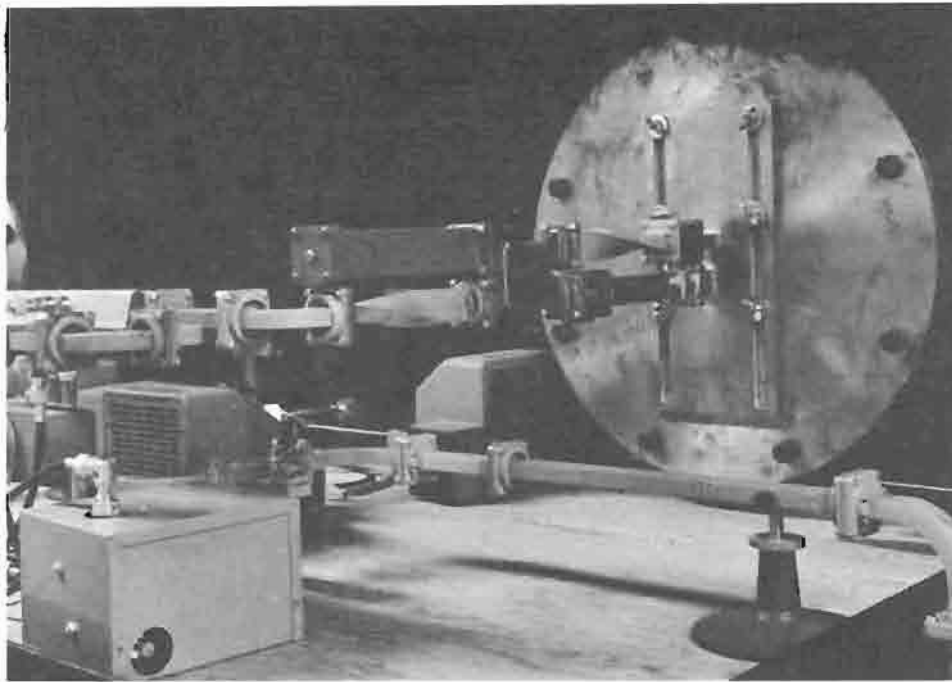
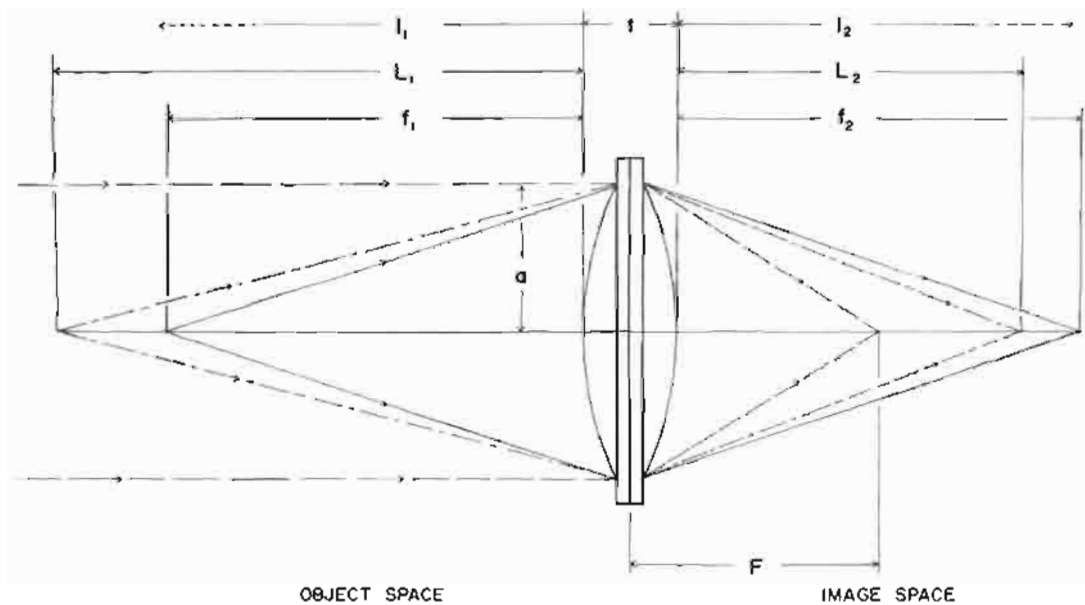


Fig. 6 Transmitter head. Note the cross-polarization of the transmitter feeds leading to the adjustable double pressure plate. The guide below the pressure plate contains the reference arm signal. The PIN Modulator is at the extreme middle left.



MICROWAVE INTERFEROMETER LENS PARAMETERS

Fig. 7 Diagram of the microwave lens with the various lens parameters defined.

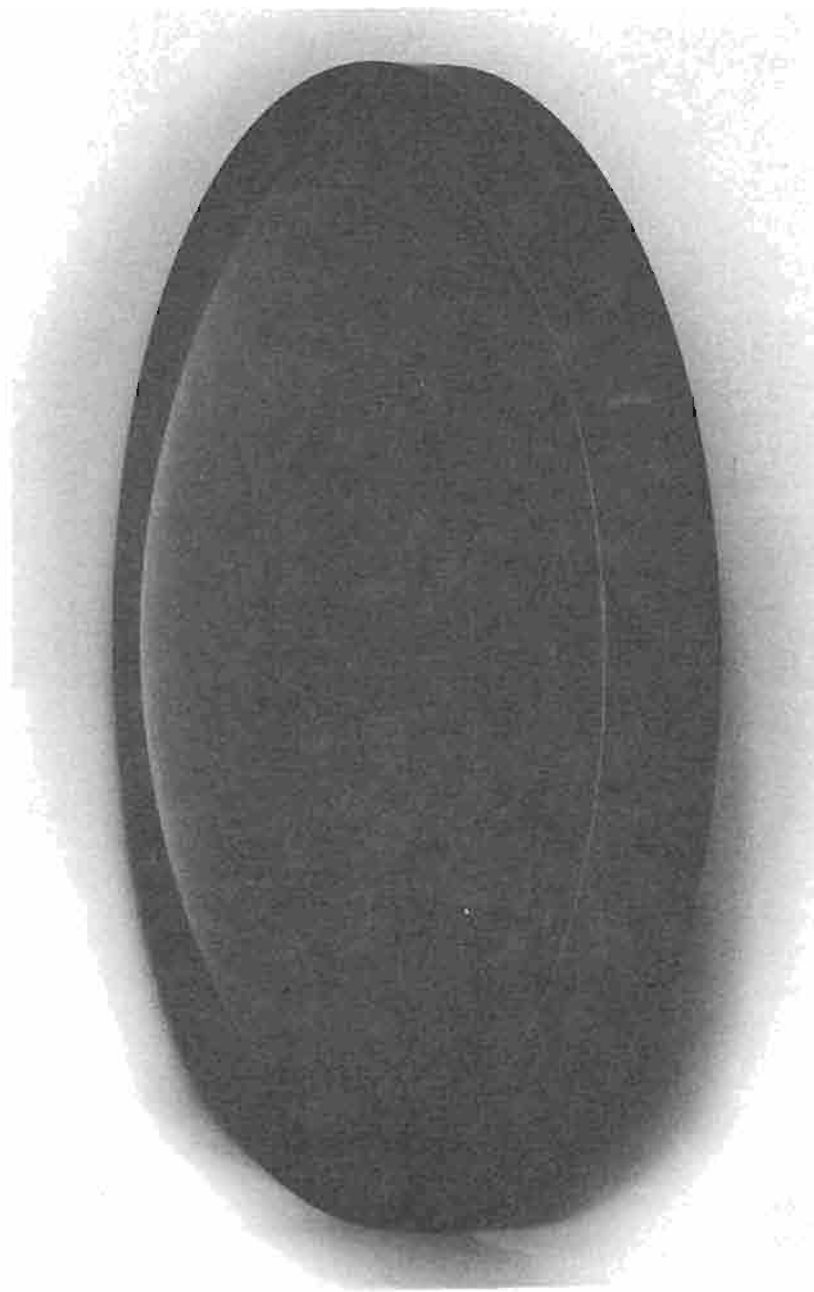


Fig. 8 Three-quarter view of one double plano-convex polystyrene microwave lens.

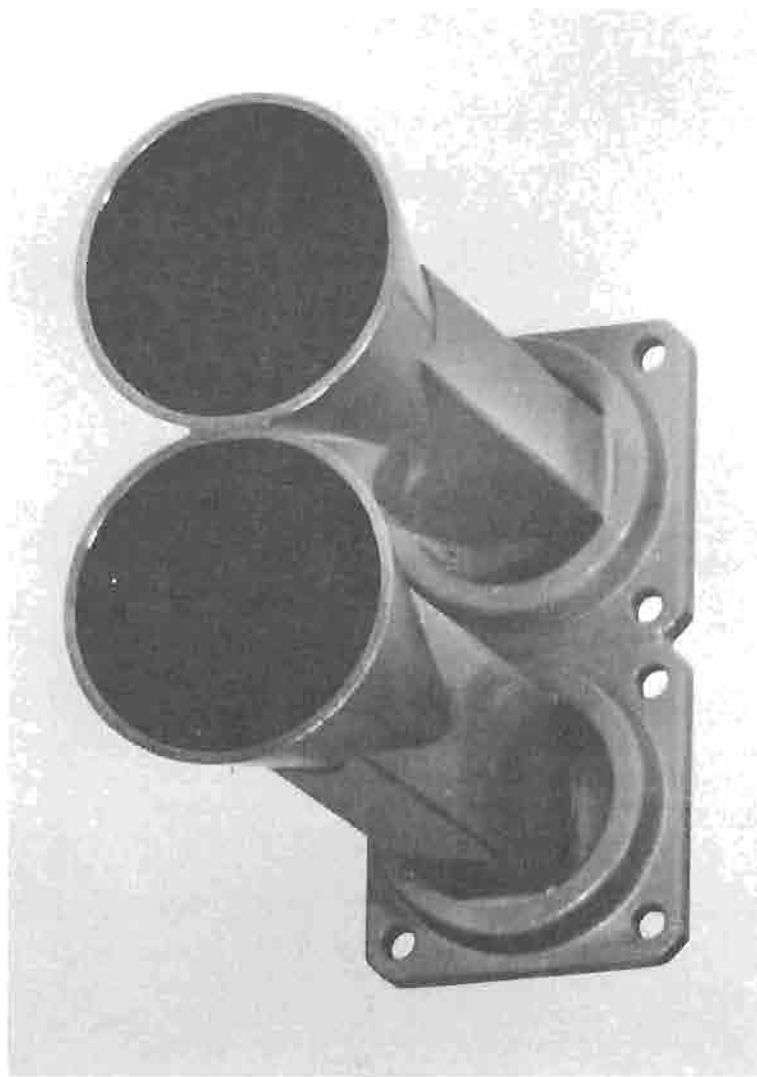


Fig. 9 Cross-polarized double conical horns for the dual-channel interferometric system.

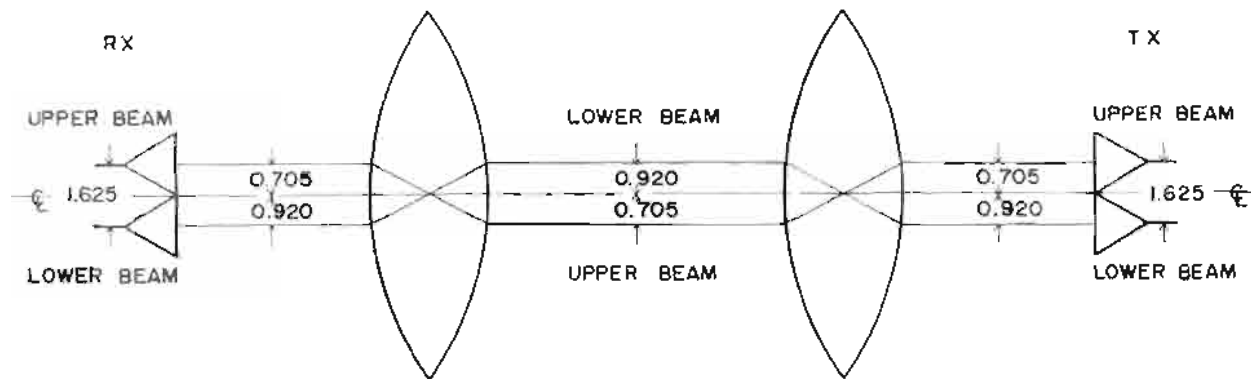


Fig. 10 This drawing illustrates how the two microwave beams are interchanged in position when passing through the center of the lens system.

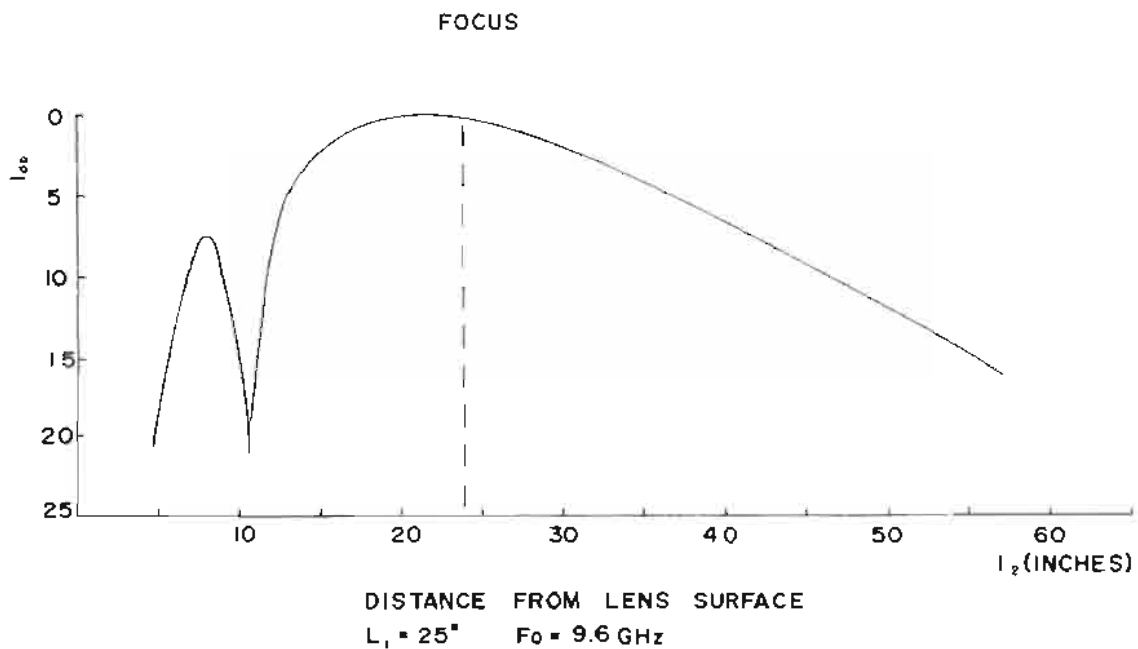


Fig. 11 Axial intensity in the image space of the 19.0 in. diameter 24.0 in. focal length lens. The distribution follows $A(\sin x/x^2)$ response.

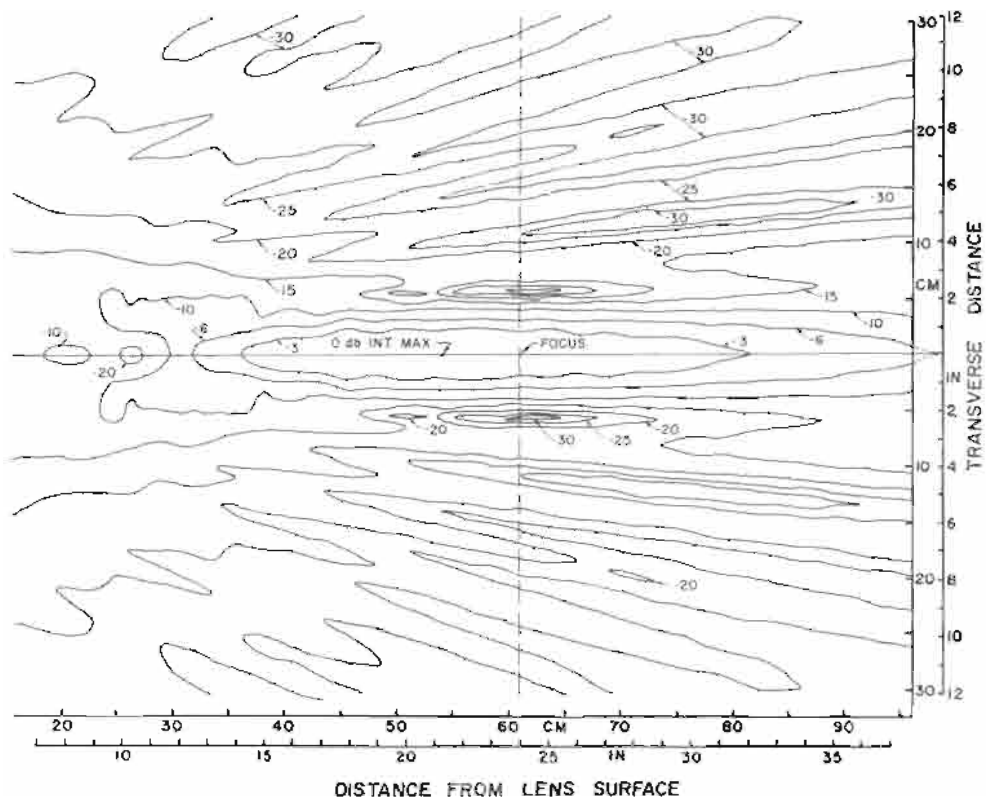


Fig. 12 Distribution of intensity in the image space of a single double plano-convex lens of 24.0 in focal length.

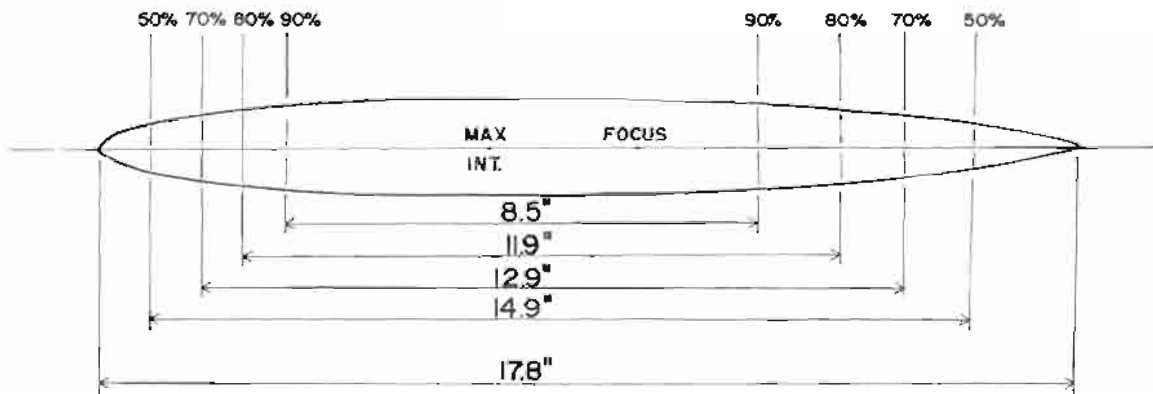


Fig. 13 Expansion of the smoothed 3 db isophote contour shown in Figure 12. For various tolerances on the width of the isophote contour, various corresponding depths-of-field can be defined.

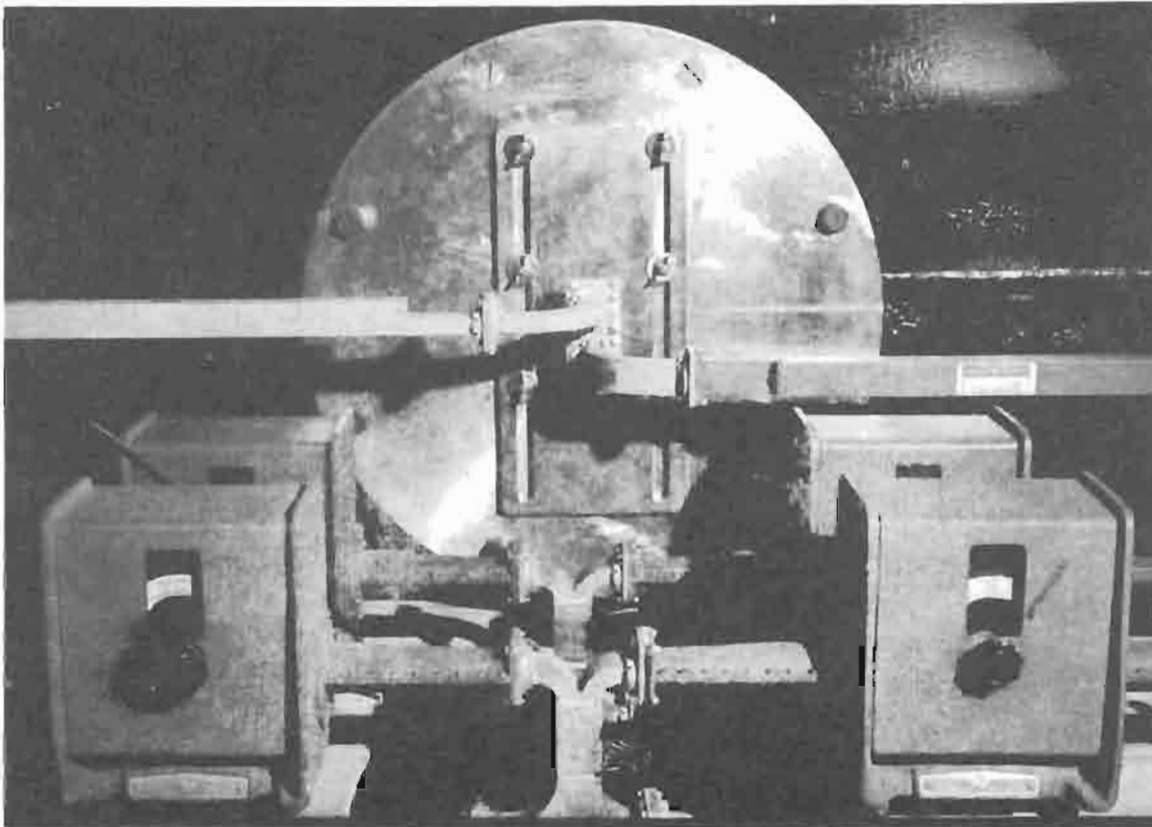


Fig. 14 Receiver head. Adjustable double pressure plate is in the center and carries the dual transmitter arms each with its top-wall power divider (top left & right). In lower center are the reference arm power dividers feeding four precision rotary phase shifters (bottom).

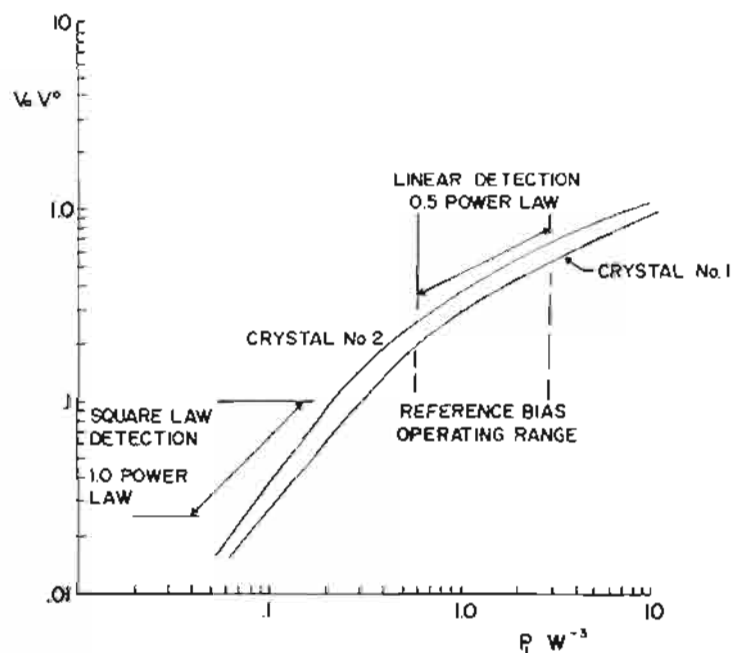


Fig. 15 Typical crystal diode response curves.



Fig. 16 Recording room showing a typical bank of Fastax recording cameras which view Tektronix 550 oscilloscopes. Polaroid recording oscilloscopes are shown at top left.

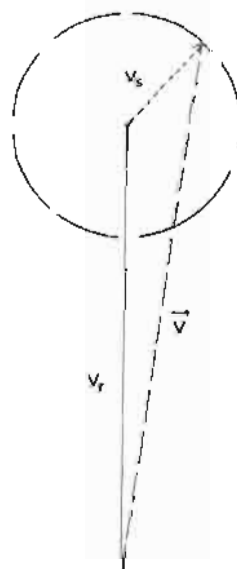


Fig. 17 Vector relationship illustrating that the reference signal is made much greater than the transmitted signal (In terms of power, the reference signal is made 100 times the level of the transmitted signal).

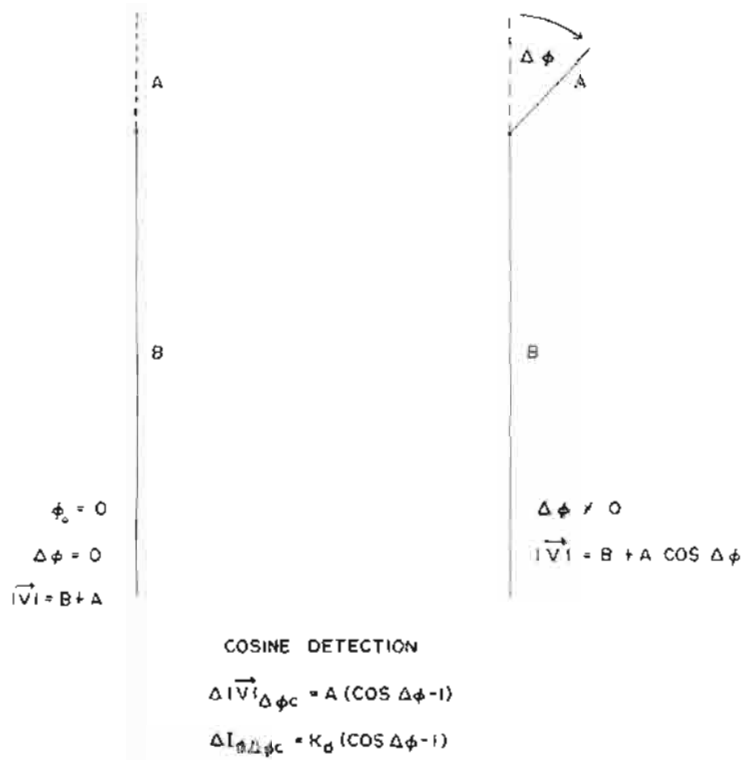


Fig. 18 Illustrating COSINE detection.

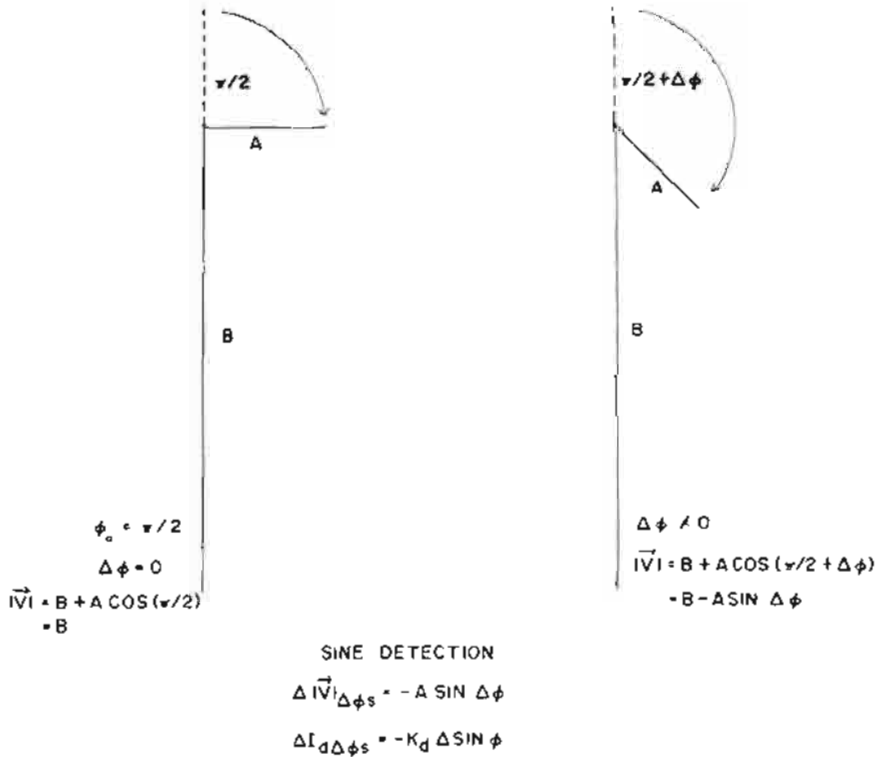


Fig. 19 Illustrating SINE detection.

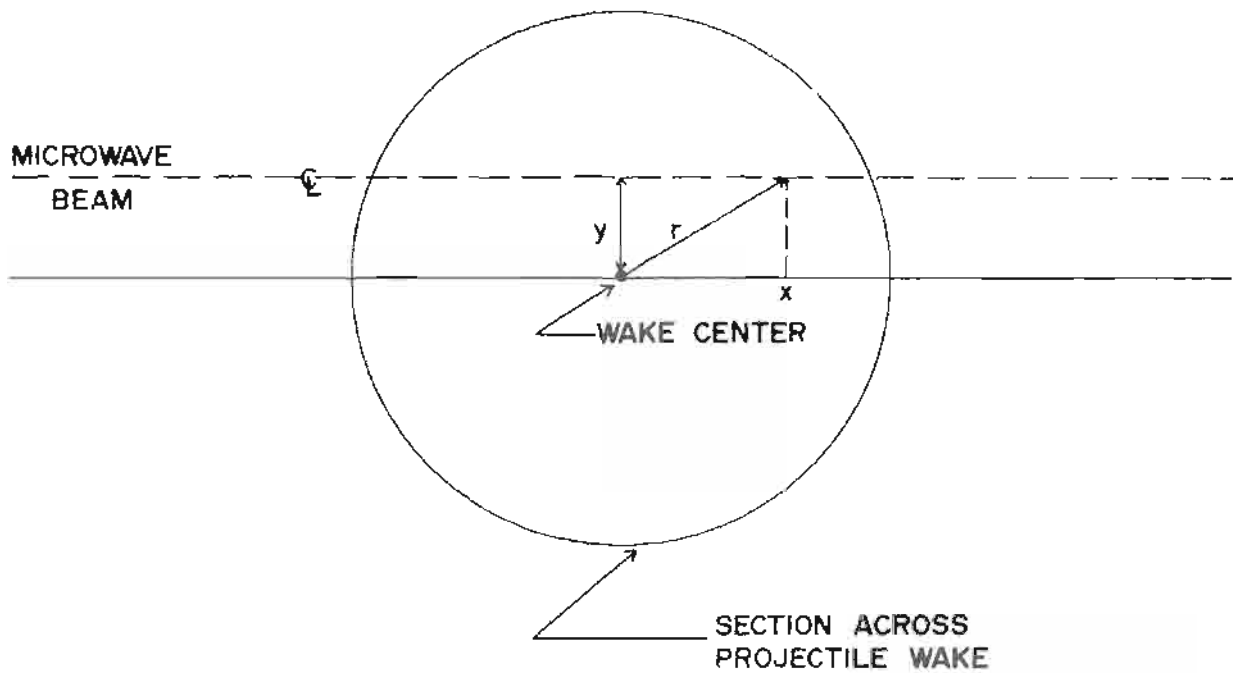
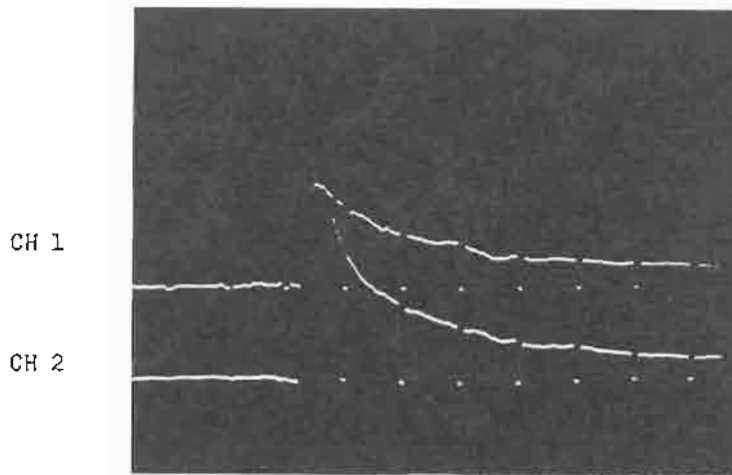
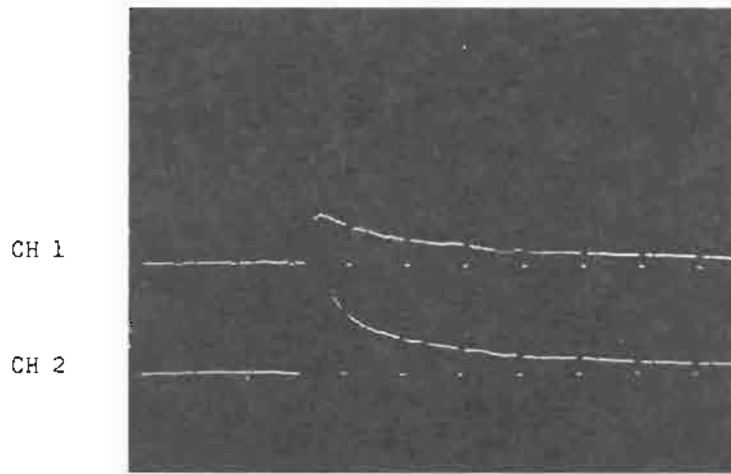
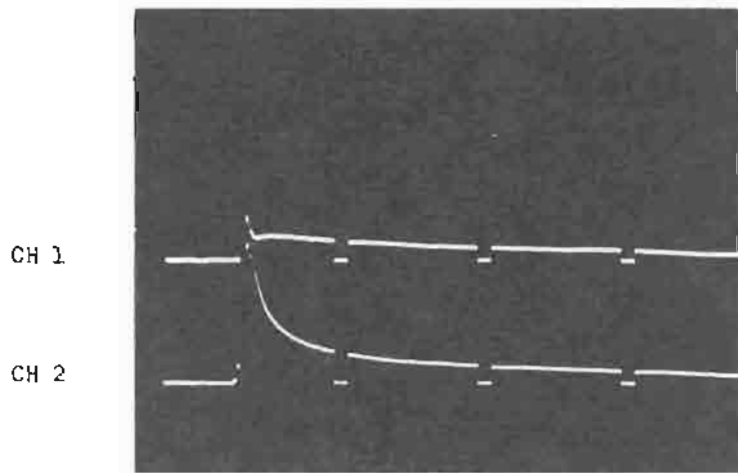


Fig. 20 Coordinate system where the microwave beam traverses the wake at a distance y from the wake center line.

ROUND	55.70
PROJECTILE	2.7" SPHERE
VELOCITY	14,600 ft/s
PRESSURE	9.9 Torr Air
INTERFEROMETER STATION	272
PROJECTILE POSITION AT STATION 272	1.50" High
DISTANCE TO UPPER BEAM (CH 2)	0.58"
DISTANCE TO LOWER BEAM (CH 1)	2.20"

Fig. 21 Typical interferometer firing report data sheet.



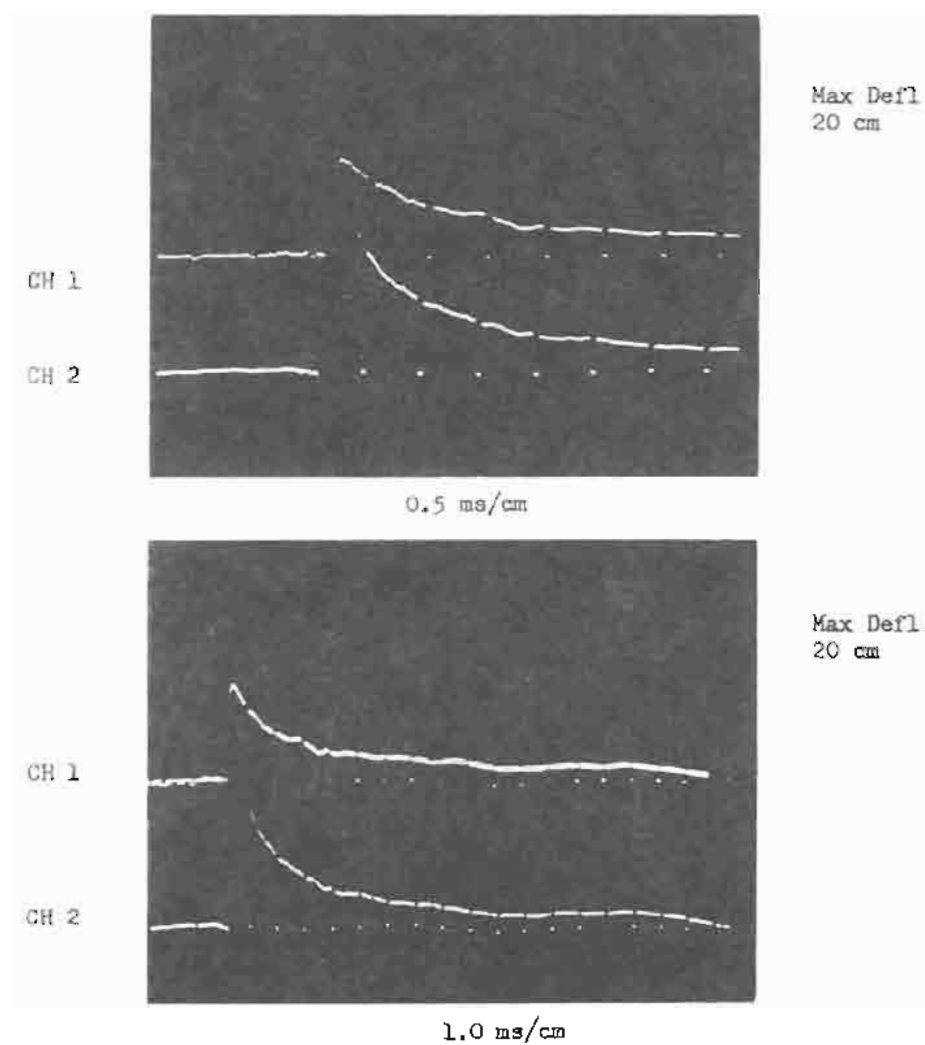


Fig. 22 Typical $\text{SIN}\phi$ displays recorded in the wake of a 2.7 in. dia. sphere launched at 14,500 ft/sec in air at 10 torr.

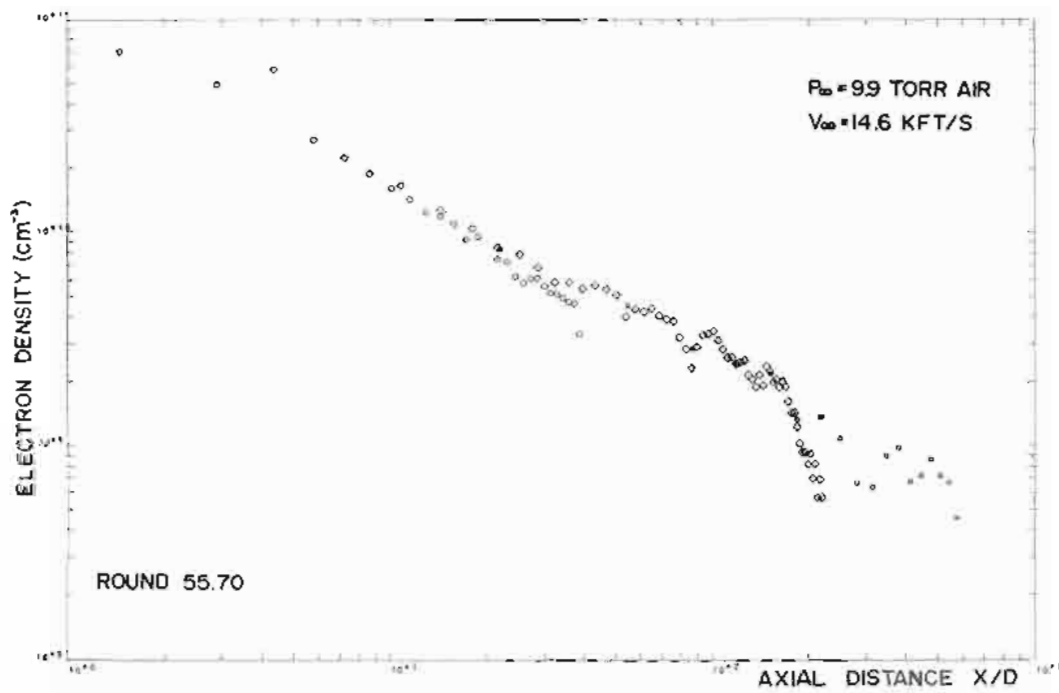


Fig. 23 Typical electron density decay on the wake axis as a function of distance behind a 2.7 in dia. sphere.

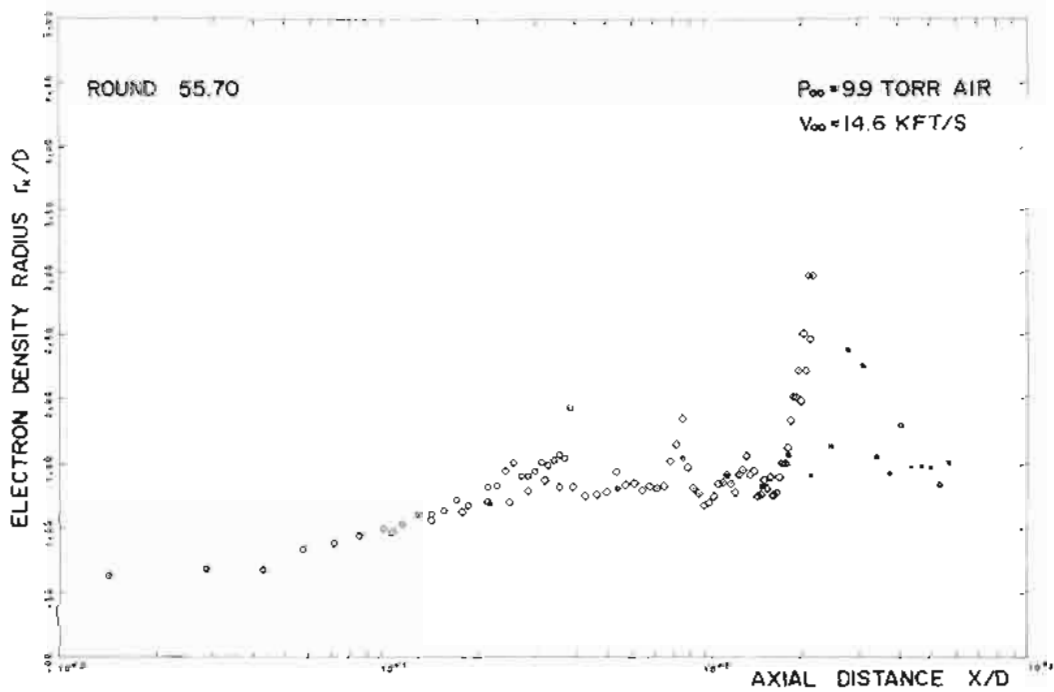


Fig. 24 Estimate of the half width of electron density radius r_n/D of the assumed gaussian distribution of electron density in the wake of a 2.7 in dia. sphere.

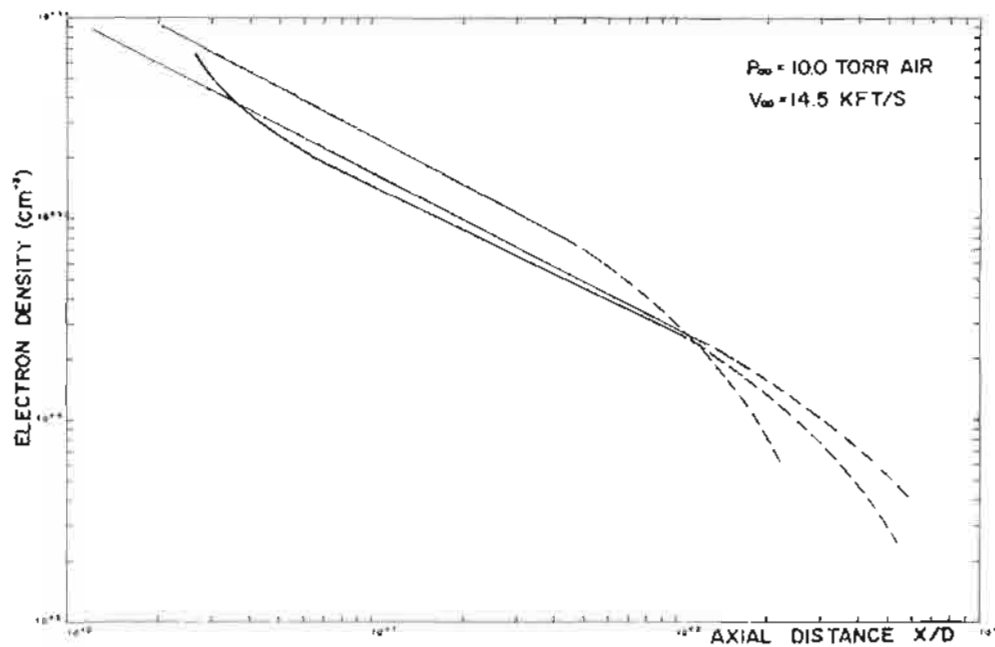


Fig. 25 Comparison of electron density decay data on 3 selected rounds.

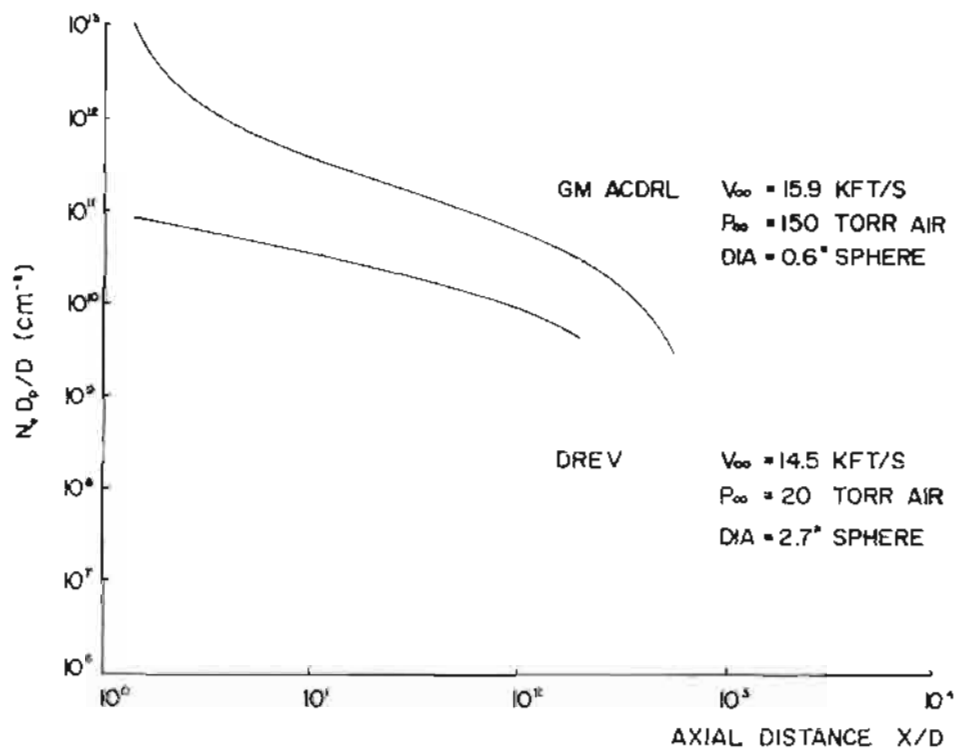


Fig. 26 Comparison of DREV and GM ACDRL exponential electron density decay data in a sphere wake.

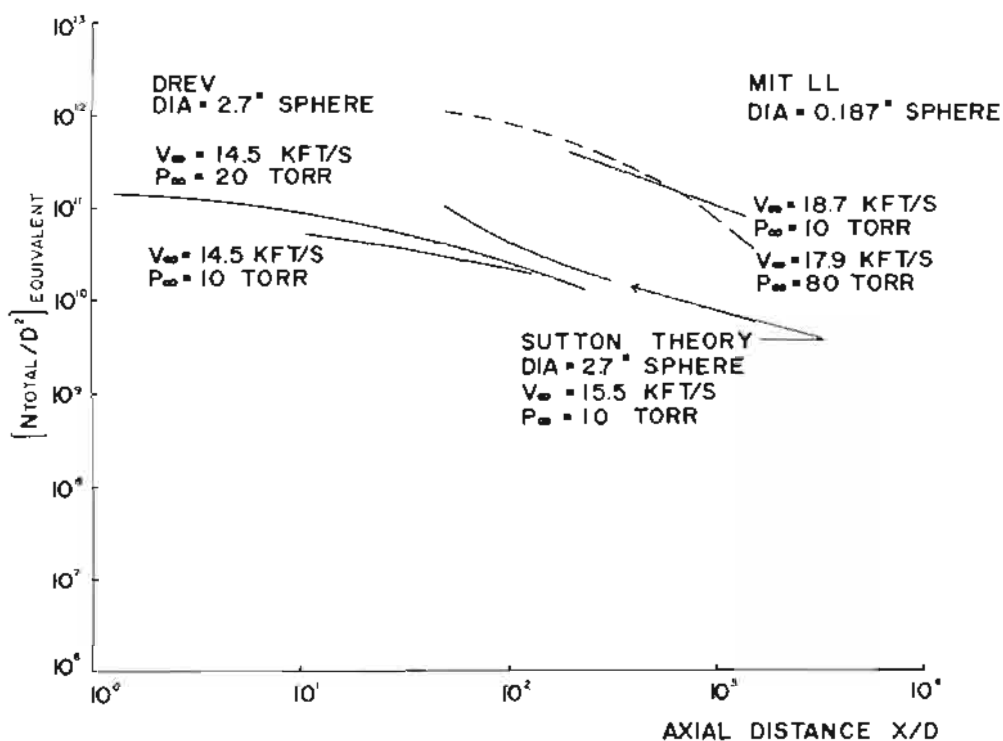


Fig. 27 Comparison of DREV and MIT LL exponential electron density decay in a sphere wake. Also shown are theoretical results calculated by Sutton.

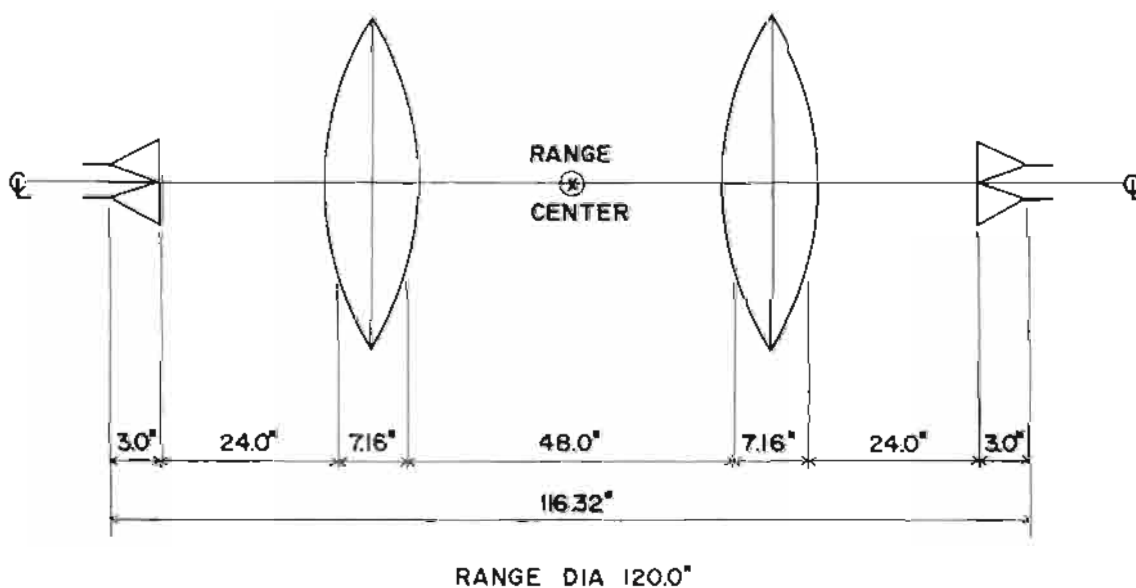


Fig. 28 Physical dimensions of Interferometric Station 272 in Range 5.

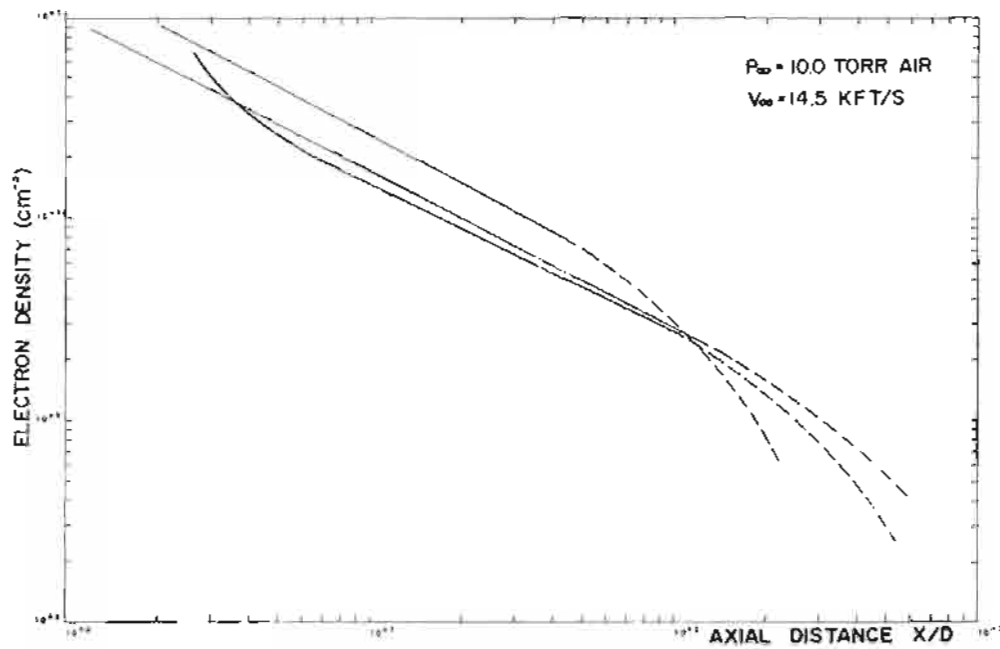


Fig. 25 Comparison of electron density decay data on 3 selected rounds.

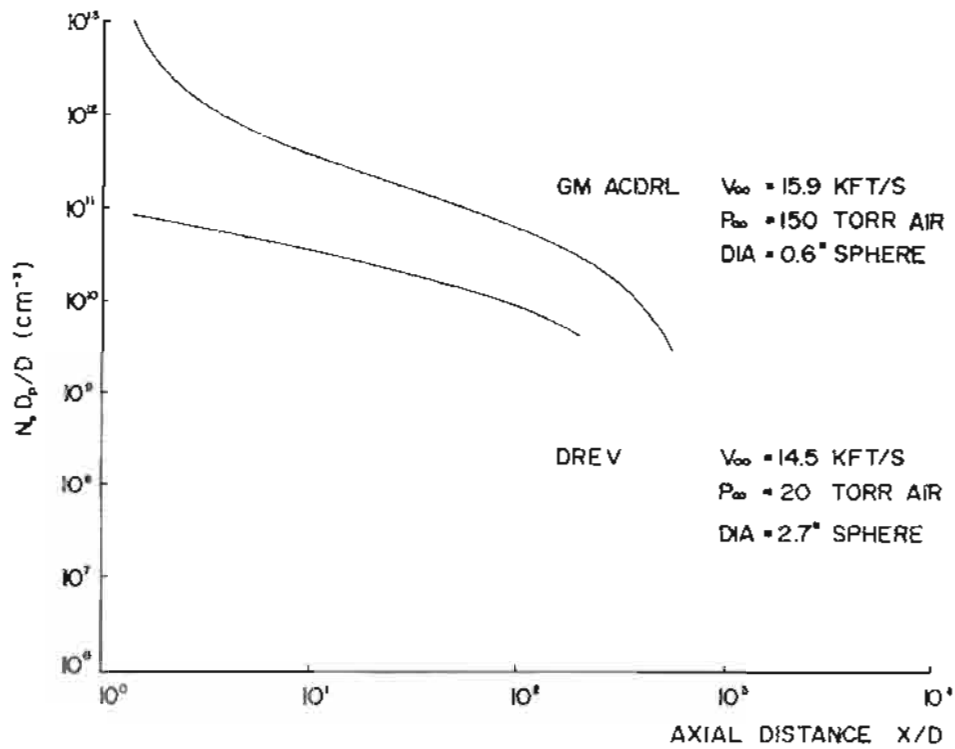


Fig. 26 Comparison of DREV and GM ACDRL exponential electron density decay data in a sphere wake.

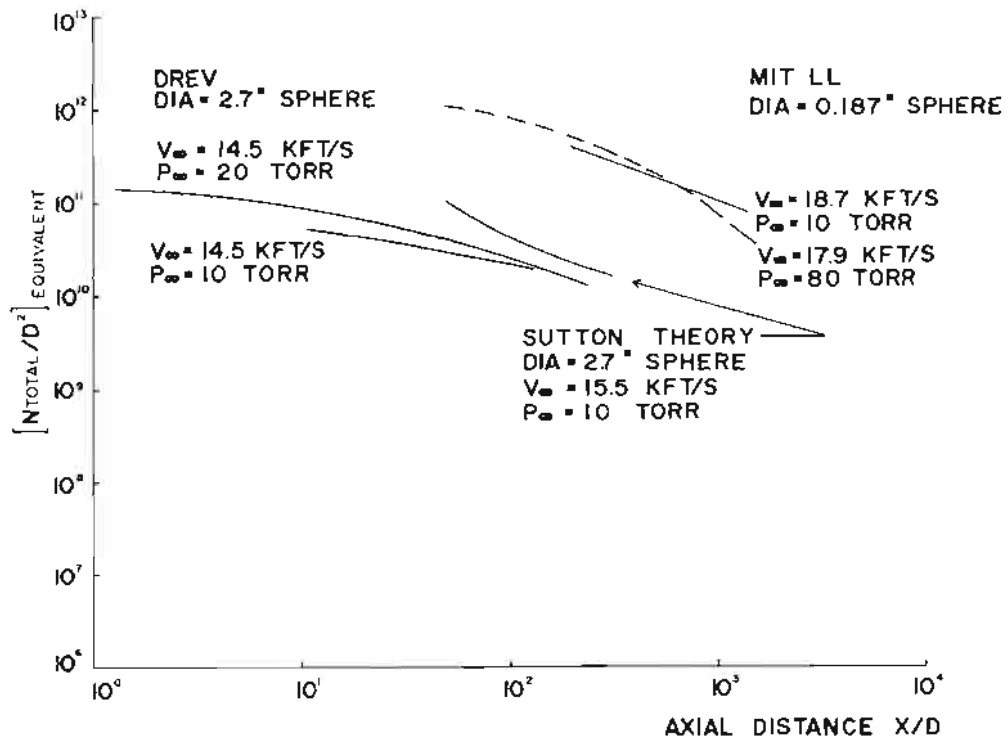


Fig. 27 Comparison of DREV and MIT LL exponential electron density decay in a sphere wake. Also shown are theoretical results calculated by Sutton.

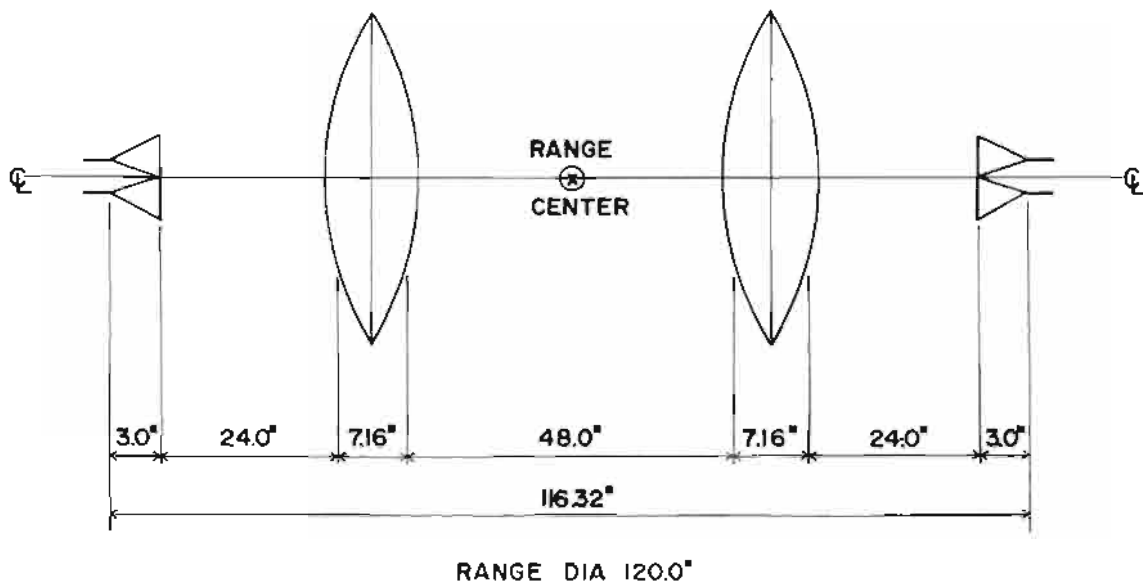


Fig. 28 Physical dimensions of Interferometric Station 272 in Range 5.

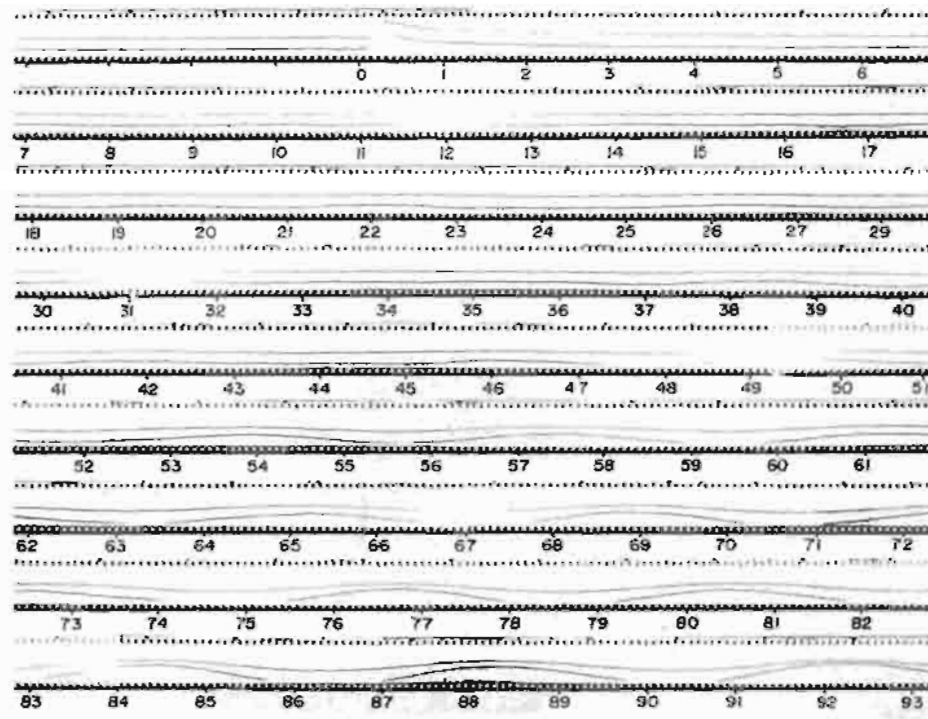


Fig. 29 Fastax film illustrating the long-wave periodic modulation disturbance of the interferometer signals due to the effect of the build-up of mechanical vibration following the launching of a projectile.

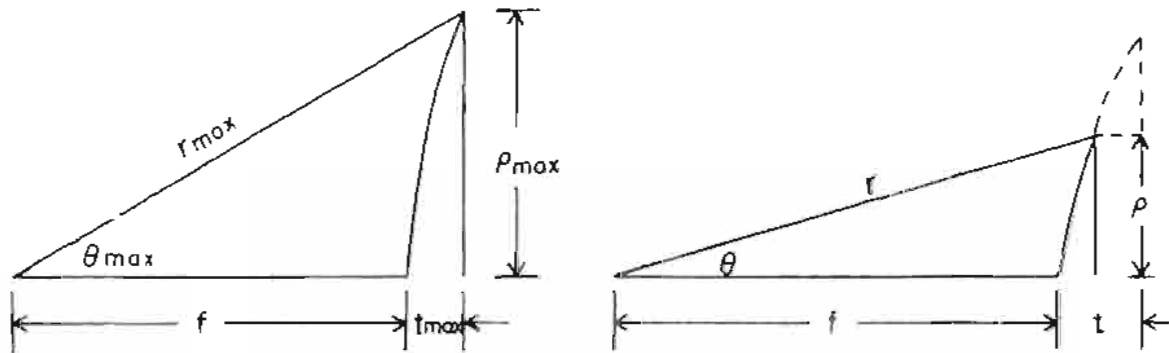


Fig. 30 Coordinate system for lens design

UNCLASSIFIED

44

APPENDIX A

Design Considerations for Dielectric Focussing Lens Systems for Range 5 Interferometer

A.1 Double Lens Focussing System

The ionization across a hypersonic wake is certainly non-uniformly distributed, while for the size of projectiles launched in ballistic ranges, the area illuminated by a standard gain horn is large compared to the size of the wake. One way of improving resolution is to use a microwave lens and to focus the microwave energy into a predetermined region of the wake. After interaction with the wake plasma, the energy must be recovered and channeled to a detector. This could be done by intercepting the energy with a large receiving horn at some short distance behind the focus. If multiple beams are to be used, this method cannot be employed, because one must ensure that the energy originating from one particular channel of the multiple source antenna is directed into the corresponding channel of the multiple receiver antenna. This appears to be readily done by using a second microwave lens, identical to the first, positioning it symmetrically relative to the focal point of the first lens (Ref. 12).

A.2 Reflected Shock Considerations

The effects of the reflection at the range walls of the bow shock system created by a hypersonic projectile travelling on a cylindrical ballistic range and the subsequent propagation of the shock wave back towards the center of the range, have been fairly well explored by recent work at DREV (Ref. 14). For example, the situation is at its worst when the reflecting shock is focussed at the range center and when a particular measuring station contains a large asymmetry in cross section. With the dielectric focussing lens system, one introduces a large pair of disk-like objects into the range about the axis and shock waves are obviously going to be reflected from these objects. On the other hand, the lenses can certainly be located symmetrically and the convexly curved surfaces are such as to contribute a defocussed reflected shock wave at the center of the range. To avoid disturbing the focussing properties of the system, one is constrained not to attempt to insert an arbitrary shock absorbing material in front of the lenses without extensive investigation. In order to permit as much undisturbed measurement time as possible, one should remove the lenses as far as possible from the flight line, since it takes time for the bow shock to propagate to the lens face, reflect and propagate back toward the range axis. Figure 28 illustrates how the present Range 5 interferometer configuration uses up the available space.

A.3 Mechanical Rigidity

Variations in path length in the transmission arm due to physical displacement of components, of necessity not rigidly held together, will be detected as phase shifts and will interfere with the measurement of phase shift contributions due to ionization in the plasma under study. The present mechanical system imposed a box-like strut system to reinforce the range cross-section and to rigidly hold the lens system to the range at the interferometer station (Fig. 5).

The system appears adequate to control any problems of vibration associated with reflected shock waves at the interferometer station, and about 10 milliseconds of analyzable signal could be recovered over the ambient pressure range of about 1 - 20 torr normally encountered. (No experience was obtained at higher pressures). Beyond 10 milliseconds, a low frequency disturbance of increasing amplitude built up in the detected phase shift. This was attributed to vibration of the whole range structure due to the impact of the projectile at the butt of the range (Fig. 29).

A.4 Scaling a Lens Design

The focussing properties of a dielectric lens may be defined in terms of the wavelength, the F-number of the lens $F_n = f/d$ and parameter α , the latter depending on the ratio of the distance of image and focus from the lens, but generally varying between 1 and 2.

$$\alpha = L_2/f = 2 \quad , \quad L_1 = L_2 = 2f.$$

(These parameters are defined in Figure 7).

The beam width (Ref. 12) is given by

$$W = \frac{49\alpha}{\pi} \lambda F_n.$$

For plasma diagnostics one would prefer to have D large which implies F_n large and W small which implies a small F_n . Obviously, compromise is required and the depth of field (Ref. 12) is defined by

$$D = K |\alpha^2 \lambda F_n^2|$$

The DREV lens preliminary design was based partially on considerations of scaling from the extensive survey of the properties of a 10.6 inch diameter lens, $F_n = 1$, made at 34.45 GHz by Carswell and Richard (Ref. 12).

They found for $F_n = 1$, $\alpha = 2$, values of beam width

$$W = 1 \text{ cm}$$

and depth of field $D = 10 \text{ cm}$ (-3 db).

If we use 9.6 GHz instead of 34.45 GHz and $F_n = 0.705$ instead of $F_n = 1$ we might expect to find a value of W

$$W_{9.6} \approx \frac{34.45}{9.6} \times 0.7 \times 1 \approx 2.5 \text{ cm}$$

$$\approx 1.0 \text{ in}$$

$$D_{9.6} \approx \frac{34.45}{9.6} \times (0.7) \times 10 \approx 17.9 \text{ cm}$$

$$\approx 7.5 \text{ in}$$

As measured in the actual system these values were found to be $W = 2.0$ inches and $D = 8.6$ inches for the -3 db contour (Ref. 13).

A.5 Detailed Lens Design

There are two relations required to define the hyperbolic lens contour used in the present lens design and in most other lenses of this type (Ref. 15, 16).

The first is the lens relation

$$r = \frac{(n-1) f}{\cos\theta - 1},$$

which specifies the profile of the lens. The second specifies the maximum dimensions of the lens.

$$r \text{ max} = \frac{f + t \text{ max}}{\cos\theta \text{ max}}$$

If we chose f and t , we can solve for $\theta \text{ max}$ and $\rho \text{ max}$

$$\cos\theta \text{ max} = \frac{f + t \text{ max}}{f + n t \text{ max}}$$

$$\rho \text{ max} = r \text{ max} \sin\theta \text{ max}$$

In the foregoing, all the variables are definable with reference to Figure 30, except for n , which is the index of refraction of the material.

An example will show how a lens design can be quickly formulated.

Suppose available geometry indicates the distance f should be 24 inches. Available material to fabricate the lens suggests the maximum value of the thickness t can be 3 inches. Then if $n = 1.6$ we have

$$\text{COS}\theta \text{ max} = \frac{f + t \text{ max}}{f + n t \text{ max}} = \frac{24 + 3}{24 + (1.6)(3)} = 0.937$$

$$\theta \text{ max} = 20^{\circ} 22'$$

$$r \text{ max} = \frac{f + t \text{ max}}{\text{COS}\theta \text{ max}} = \frac{27}{0.937} = 28.8$$

$$\theta \text{ max} = 28.8 \text{ SIN}\theta \text{ max} = 10.02$$

$$= 20.04$$

$$F = f = 12.0 \text{ inches}$$

$$F_n = f/d = 0.6$$